



Integrating electrophilic and nucleophilic dual sites on heterogeneous bimetallic phosphide via enhancing interfacial electronic field to boost hydrazine oxidation and hydrogen evolution

Shucong Zhang^a, Canhui Zhang^a, Xusheng Zheng^b, Ge Su^a, Huanlei Wang^a, Minghua Huang^{a,*}

^a School of Materials Science and Engineering, Ocean University of China, 238 Songling Road, Qingdao 266100, China

^b National Synchrotron Radiation Laboratory (NSRL), University of Science and Technology of China, 433 of Huangshan Road, Hefei 230029, China

ARTICLE INFO

Keywords:

Heterogeneous bimetallic phosphides
Nitrogen doping
Interfacial electric field
Electro/nucleophilic sites
Hydrazine-assisted hydrogen production

ABSTRACT

Integrating dual sites of hydrazine oxidation reaction (HzOR) and hydrogen evolution reaction (HER) into a catalyst is highly desirable for energy-saving hydrogen production but remains challenges. Herein, we fabricate a heterogeneous nanowire array consisting of CoP and N-doped Ni₅P₄ on carbon fiber paper (N-Ni₅P₄@CoP/CFP), in which the N atoms can be selectively incorporated into Ni₅P₄ to change the Ni coordination that can regulate interfacial electronic field and thus improve the charge transfer from CoP to N-Ni₅P₄. Such an interfacial charge redistribution can induce the formation of well-defined electrophilic and nucleophilic sites, which could optimize hydrazine dehydrogenation kinetics and hydrogen adsorption free energy (ΔG_{H^+}), thus achieving splendid HzOR and HER activities. The commercial solar cells and homemade lemon batteries driven overall hydrazine splitting (OHZS) electrolyzer inspires its practical applications. Integrating the electrophilic and nucleophilic dual sites via interfacial electronic field regulation provides a new inspiration for efficiently catalyzing HzOR and HER.

1. Introduction

Overall water splitting (OWS) for high-purity hydrogen generation is greatly hindered by the thermodynamically unfavorable anodic oxygen evolution reaction (OER, $4OH^- \rightarrow O_2 + 2H_2O + 4e^-$, 1.23 V vs RHE) and cathodic hydrogen evolution reaction (HER, $2H_2O + 2e^- \rightarrow H_2 + 2OH^-$), resulting in the high operating voltage (>1.8 V) and low energy conversion efficiency [1]. Nowadays, overall hydrazine splitting (OHZS), consisting of the anodic hydrazine oxidation reaction (HzOR, $N_2H_4 + 4OH^- \rightarrow N_2 + 4H_2O + 4e^-$, -0.33 V vs RHE) and the cathodic HER, is becoming a promising approach to replace OWS for energy-saving H₂ production because of its much lower theoretical cell voltage as well as the higher safety with only byproduct of N₂ at the anode [2,3]. Some pioneering works have been devoted to developing the high-efficient bifunctional catalysts in this domain, such as PW-Co₃N, Mo-Ni₃N/Ni/NF, Cu₁Ni₂-N, Ni-C HNSA, and so on [4–11]. Nevertheless, several tough issues are highly required to be concerned. Firstly, the extra energy for H₂ production is needed to be consumed as the two-electrode OHZS electrolyzer suffers from much higher cell voltages than theoretical value. Secondly, the development of bifunctional catalysts is still at the current infant stage because of the quite different

reaction intermediates in HER and HzOR process, let alone the rational catalyst design with precise determination of active sites. Last but not least, it is necessary to deeply decipher the underlying HER and HzOR mechanism for establishing the relationship between structure and activity. Undoubtedly, a sizeable margin still exists for developing high-performance catalysts toward both HER and HzOR.

Recently, heterogeneous bimetallic phosphides (such as Ni₂P/CoP [12], Ni₂P-Cu₃P [13], and FeP/Ni₂P [14]), constructed by interface engineering, have been demonstrated as advanced catalysts toward HER or HzOR owing to high intrinsic catalytic activity, tunable composition and structure, and high electronic conductivity [15–17]. The interface interaction between the heterogeneous components with different energy levels can not only intelligently create spontaneous polarization electric fields for providing the electronic migration potential, but also effectively build numerous charge transfer channels for shortening the electronic migration path [18,19]. However, most of obtained catalysts are not capable of possessing excellent bifunctionality toward both HER and HzOR due to the incompatibility of active sites for corresponding reactions. It is generally accepted that the catalytic performance is closely associated with the adsorption behavior of reaction intermediates on the active sites [20,21]. For cathodic HER, hydrogen

* Corresponding author.

E-mail address: huangminghua@ouc.edu.cn (M. Huang).

<https://doi.org/10.1016/j.apcatb.2022.122207>

Received 31 August 2022; Received in revised form 21 October 2022; Accepted 22 November 2022

Available online 1 December 2022

0926-3373/© 2022 Elsevier B.V. All rights reserved.

intermediates produced by water dissociation process are generally adsorbed on nucleophilic sites [22]. For anodic HzOR, the N atoms with lone-pair electrons in adsorbed N_2H_4^* molecules prefer to interact with the electrophilic sites [23]. The efficient integration of electrophilic and nucleophilic centers into a single catalyst should be beneficial to achieve HER and HzOR simultaneously. However, it is difficult to achieve the formation of well-defined nucleophilic and electrophilic sites in heterogeneous bimetallic phosphides, because the interface electric field only caused by the inherent energy level difference between the two components is not strong enough [24]. It is highly desirable for further tailoring the energy level structure to accelerate migration of positive and negative charges along opposite directions. Recent studies have showed that the incorporation of light N element into the lattices of single metal phosphides can modify the energy level structure and boost the catalytic performance without perturbing the crystal structure [25]. It is expected that such doping can enlarge the difference in energy level to enhance interfacial electric field for heterogeneous bimetallic phosphides, and thus effectively speeding up the charge transfer process to generate the corresponding electrophilic and nucleophilic sites. Unfortunately, few reports have been presented on the N incorporation into heterogeneous bimetallic phosphides for constructing such dual sites to catalyze high-performance HER and HzOR simultaneously. Moreover, the deep insight into the underlying catalytic mechanism of electrophilic and nucleophilic sites is essential for the rational design of high-efficient bifunctional catalysts toward hydrazine-assisted H_2 production but remains unexplored.

Herein, a coupling hydrothermal-phosphorization strategy is adopted to ingeniously construct heterogenous nanowire array consisting of CoP and N-doped Ni_5P_4 on carbon fiber paper (denoted as N- Ni_5P_4 @CoP/CFP). Notably, the selective incorporation of guest N into the host Ni_5P_4 can lead to the adjustment of Ni coordination structure, and the energy level structure of Ni_5P_4 can thus be fine-regulated to enhance interfacial electric field for facilitating charge transfer from CoP to N- Ni_5P_4 . Density functional theory (DFT) calculations reveal that such a charge redistribution is in favor of not only forming the nucleophilic P sites with balanced H^* adsorption/desorption in N- Ni_5P_4 for catalyzing HER, but also yielding the electrophilic Co sites with favorable N_2H_4^* dehydrogenation in CoP for catalyzing HzOR. The sufficient electrophilic Co sites as well as the abundant nucleophilic P sites can be integrated into the N- Ni_5P_4 @CoP/CFP, and hence the excellent catalytic performance can be obtained toward both HER and HzOR. To be specific, it only needs the ultralow HER overpotentials of 55, 56, and 59 mV to reach a current density of 10 mA cm^{-2} in acid, alkaline, and neutral media, respectively. In the meantime, a low HzOR potential of mere -32 mV is required to achieve 10 mA cm^{-2} in alkaline electrolyte, outperforming those of most previous reported catalysts. More importantly, a two-electrode OHZS electrolyzer (the N- Ni_5P_4 @CoP/CFP as both anode and cathode catalysts) merely needs the cell voltage as low as 0.037 V to drive the current density of 10 mA cm^{-2} , which is much less than that of the OWS system, outperforming the most recently reported OHZS electrolyzers. Furthermore, a sustainable H_2 production system is explored by using a commercial solar cell and a home-made lemon battery as power sources to drive OHZS electrolyzer, where the promising H_2 generation rates of 1.141 and $0.056 \text{ mmol cm}^{-2} \text{ h}^{-1}$ can be obtained, implying the great potential for energy-saving H_2 production. This work provides an encouraging inspiration to rationally designing efficient catalysts toward hydrazine-assisted H_2 production via integrating electro/nucleophilic sites into heterogeneous bimetallic phosphides.

2. Experimental section

2.1. Synthesis of N- Ni_5P_4 @CoP/CFP, N- Ni_5P_4 /CFP, and CoP/CFP

The N- Ni_5P_4 @CoP/CFP is synthesized via a coupling strategy involving hydrothermal synthesis and phosphorization treatment.

Firstly, a piece of CFP ($2.5 \text{ cm} \times 4 \text{ cm}$) is cleaned with concentrated nitric acid, and then washed with deionized acetone, ethanol, and deionized water. Next, the $4 \text{ mmol Co}(\text{NO}_3)_2 \cdot 6 \text{ H}_2\text{O}$, 2 mmol urea , and $1 \text{ mmol NH}_4\text{F}$ are dissolved in 20 mL deionized water under vigorous stirring for 30 min . The cleaned CFP is immersed in the above solution, and then transferred into a Teflon-lined stainless steel autoclave and heated at 120°C for 12 h . After cooling down naturally at room temperature, the sample is then taken out and then washed by ethanol and deionized water. The CFP coated with cobalt hydroxy carbonate [$\text{Co}(\text{CO}_3)_{0.5}\text{OH} \cdot 0.11 \text{ H}_2\text{O}$] precursor (named as Co/CFP) is washed by ethanol and deionized water, and dried in a 60°C oven overnight. The obtained Co/CFP is immersed in 20 mL alcohol solution with $1 \text{ mmol Ni}(\text{NO}_3)_2 \cdot 6 \text{ H}_2\text{O}$ and 5 mmol urea , and then transferred into a Teflon-lined stainless steel autoclave and heated at 90°C for 6 h . After cooling down, the Ni-hydroxide layer covered Co/CFP (named as Ni@Co/CFP) precursor is taken out and washed by deionized water, and then fully dried in 60°C oven. Then, the N- Ni_5P_4 @CoP/CFP is finally obtained by a common phosphorization process of above-prepared Ni@Co/CFP at the temperature of 400°C for 1 h . The N- Ni_5P_4 /CFP is prepared in the same way as N- Ni_5P_4 @CoP/CFP except that the Co/CFP precursor is replaced by the CFP. The synthesis of CoP/CFP is similar to that of N- Ni_5P_4 @CoP/CFP except that the Ni@Co/CFP is replaced by the Co/CFP precursor in phosphorization process.

2.2. Materials characterization

The morphology characterization is performed by scanning electron microscopy (SEM, Zeiss SUPRA 55 Sapphire) and transmission electron microscopy (TEM, FEI Talos 200 S). X-ray diffraction (XRD) measurements are conducted on a Bruker D8 ADVANCE diffractometer with a monochromated Cu K α radiation. Raman spectra are collected on the Thermo Fisher spectrometer equipped with helium-neon (633 nm) and argon (532 nm) lasers. X-ray photoelectron spectroscopy (XPS) is performed on Thermo Scientific ESCALAB Xi+. Ultraviolet photoelectron spectroscopy (UPS) is performed on Thermo ESCALAB Xi+ equipped with ultraviolet photoelectron spectrometer (Hel (21.22 eV)). Brunauer-Emmett-Teller (BET) surface area is measured by using Micromeritics TriStar II 3020 volumetric adsorption analyzer at 77 K . The X-ray absorption spectra (XAS) including X-ray absorption near-edge structure (XANES) and extended X-ray absorption fine structure (EXAFS) at Co K-edge and Ni K-edge of the samples are recorded at the beamline BL14W1 of Shanghai Synchrotron Radiation Facility (SSRF) in China.

2.3. Electrochemical characterization

All electrochemical measurements of the catalysts are performed with using an electrochemical workstation (Biologic SP-300, France). In a typical three-electrode system, the as-synthesized catalysts, graphite rod and saturated calomel electrode are employed as the working electrode, the counter electrode and reference electrode respectively. All potentials in this study are converted to RHE reference according to the equation of $E_{\text{RHE}} = E_{\text{SCE}} + 0.241 + 0.059 \text{ pH}$. All the measured potentials are calibrated with 90% iR compensation if not explicitly specified. The linear sweep voltammetry (LSV) is performed at a scan rate of 5 mV s^{-1} . The Tafel slope is obtained by Tafel equation [$\eta = b \log(j) + a$]. Electrochemical impedance spectroscopy (EIS) spectra are recorded at a selected potential in the frequency range from 100 kHz to 0.01 Hz .

2.4. Computational methods

All the calculations are performed within the framework of the density functional theory (DFT) as implemented in the Vienna Ab initio Software Package (VASP 5.3.5) code within the Perdew-Burke-Ernzerhof (PBE) generalized gradient approximation and the projected augmented wave (PAW) method. The cutoff energy for the plane-wave basis set is set to 450 eV . The Brillouin zone of the surface unit cell is

sampled by Monkhorst-Pack (MP) grids, with a k-point mesh for catalysts structure optimizations. The surfaces of CoP, Ni_5P_4 , $\text{N-Ni}_5\text{P}_4$ and $\text{N-Ni}_5\text{P}_4 @ \text{CoP}/\text{CFP}$ are determined by $6 \times 6 \times 1$, $5 \times 3 \times 1$, and $2 \times 2 \times 1$ Monkhorst-Pack grid. The convergence criterion for the electronic self-consistent iteration and force is set to 10^{-5} eV and 0.01 eV/Å, respectively. A vacuum layer of 15 Å is introduced to avoid interactions between periodic images.

3. Results and discussion

3.1. Synthesis and characterization

The $\text{N-Ni}_5\text{P}_4 @ \text{CoP}/\text{CFP}$ is achieved by a coupling strategy involving the hydrothermal synthesis and subsequent phosphorization treatment, as schematically displayed in Fig. 1a. First, the Co-carbonate hydroxides nanowires array is directly grown on the CFP (denoted as Co/CFP) through a well-developed hydrothermal method [26]. The Ni-hydroxide layer covered on the surface of nanowires (denoted as the $\text{Ni} @ \text{Co}/\text{CFP}$) is then obtained by the further hydrothermal synthesis, in which urea as the nitrogen source may bond with the Ni atoms [27]. Finally, the 400 °C

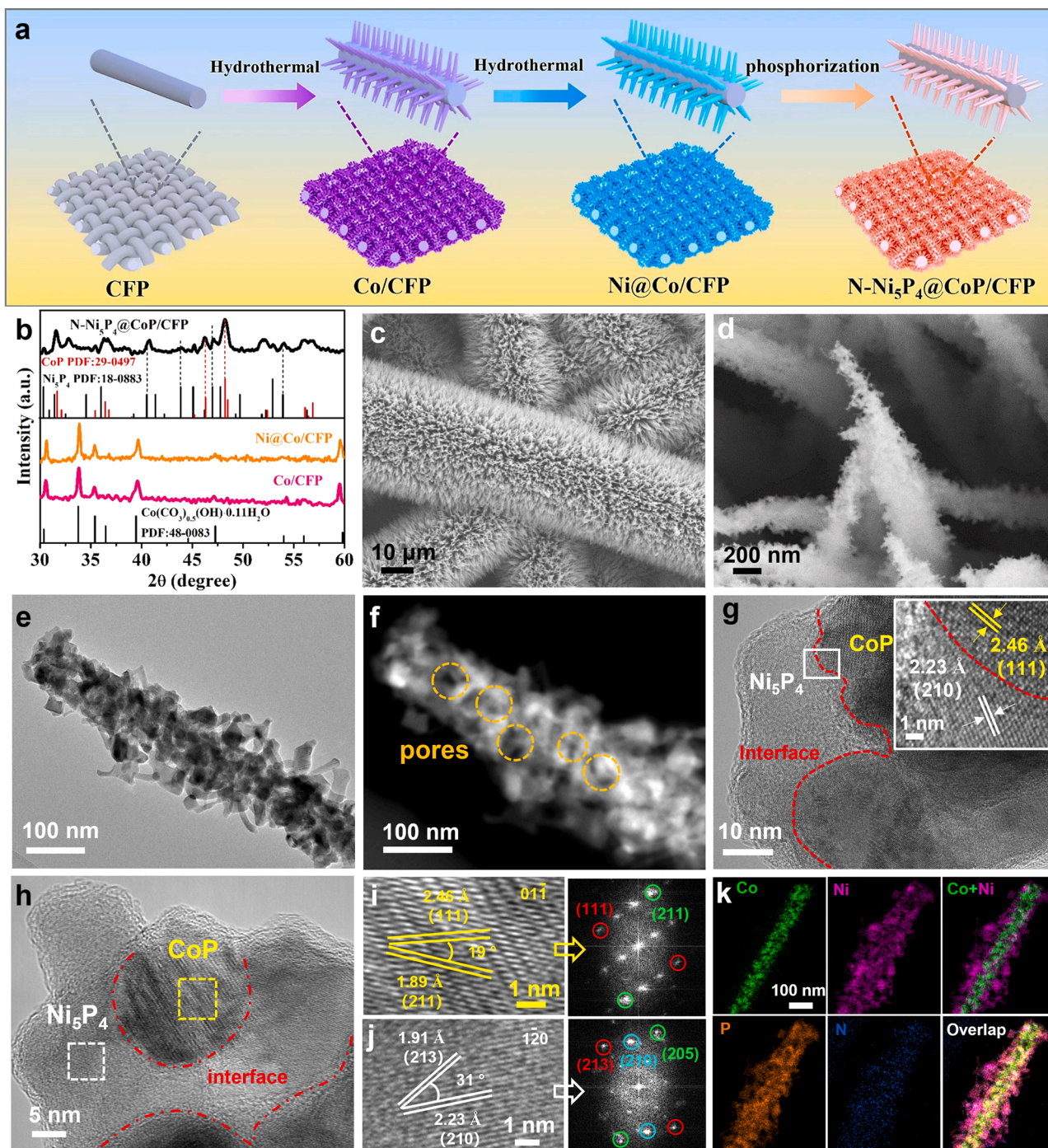


Fig. 1. (a) Schematic illustration of the synthesis process for $\text{N-Ni}_5\text{P}_4 @ \text{CoP}/\text{CFP}$. (b) XRD patterns of Co/CFP, Ni@Co/CFP, and $\text{N-Ni}_5\text{P}_4 @ \text{CoP}/\text{CFP}$. (c, d) SEM, (e) TEM, (f) HAADF-STEM, (g-j) HRTEM, and (k) EDS elemental mapping images of $\text{N-Ni}_5\text{P}_4 @ \text{CoP}/\text{CFP}$.

is collected as optimized temperature to directly phosphatize the Ni@Co/CFP precursor for preparing the target N-Ni₅P₄ @CoP/CFP under Ar atmosphere (Fig. S1). Powder X-ray diffraction (XRD) is performed to provide the component information of the Co/CFP, Ni@Co/CFP and N-Ni₅P₄ @CoP/CFP. As shown in Fig. 1b, the diffraction peaks can be observed at 17.5, 26.7, 33.8, 35.4 and 47.3° for the Co/CFP and Ni@Co/CFP, which are attributed to the (020), (220), (221), (040) and (340) planes of Co(CO₃)_{0.5}OH·0.11 H₂O (PDF No. 48-0083), respectively. There are no new diffraction peaks for the Ni@Co/CFP, suggesting that the Ni-hydroxide layer grown onto Co(CO₃)_{0.5}OH·0.11 H₂O nanowires may exist as amorphous state. Interestingly, along with the phosphorization, a series of new diffraction peaks appear for the N-Ni₅P₄ @CoP/CFP. The peaks at 30.4, 40.6, 47.0, 47.8, 53.0 and 54.0° can be indexed into (200), (210), (301), (213), (214) and (220) planes of hexagonal Ni₅P₄ (PDF No. 18-0883), whereas the peaks at 31.6, 35.3, 36.3, 46.2, 56.0 and 56.8° are ascribed to the (011), (200), (112), (211), (020) and (301) of orthorhombic CoP (PDF No. 29-0497). Notably, compared to the corresponding peaks in standard PDF card, the characteristic peaks shift slightly for Ni₅P₄ phase, whereas there is no shift for those of CoP phase, demonstrating that N is doped into Ni₅P₄ rather than CoP. The above analysis suggests that the N-Ni₅P₄@CoP heterostructure nanowire array is successfully fabricated grown on CFP.

The morphological structures of the Co/CFP, Ni@Co/CFP and N-Ni₅P₄ @CoP/CFP are explored by scanning electron microscopy (SEM). A smooth surface can be observed on the Co(CO₃)_{0.5}OH·0.11 H₂O nanowire array for the Co/CFP, whereas Ni-hydroxide layer with rough dendrite structure is covered on the nanowires surface for the Ni@Co/CFP (Fig. S2). Interestingly, the nanowire array with dendritic structure could be well-retained for the N-Ni₅P₄ @CoP/CFP after phosphorization treatment (Fig. 1c), which are highly oriented and vertically rooted on the carbon fiber with distinctive gaps between nanowires (Fig. 1d). The above well-aligned nanowire array of the N-Ni₅P₄ @CoP/CFP could have the strong capillary force for absorbing liquid phase electrolyte onto the nanowire surface, which can not only endow the catalyst with more accessible active sites, but also reduce gas-solid contact region for the acceleration of bubbles release [28]. As a proof-of-concept, the surface wettability of the as-prepared N-Ni₅P₄ @CoP/CFP is investigated by contact angle measurements (Fig. S3). The N-Ni₅P₄ @CoP/CFP exhibits the superior hydrophilicity and aerophobicity, which are evidenced by a nearly 0° of water contact angle and large bubble contact angle of 142°, respectively. Therefore, it is reasonably believed that this deployed architecture can benefit to the water adsorption and bubbles release for enhancing mass transfer, and thus be preponderant in facilitating the reaction kinetics and reducing the actual operating voltage. Transmission electron microscopy (TEM) images of the N-Ni₅P₄ @CoP/CFP present that the surface of the nanowire is composed of abundant dendritic structures with irregularity in size (Fig. 1e). The pore size and surface area of the N-Ni₅P₄ @CoP/CFP are studied by N₂ sorption measurement (Fig. S4), in which the Brunauer-Emmett-Teller (BET) specific surface area and the average pore diameter are determined to be 31.77 m²g⁻¹ and 7 nm, respectively. The porous structure can also be clearly discovered on the nanowires surface in the high-angle annular dark-field scanning TEM (HAADF-STEM) image (Fig. 1f). Such a hierarchical porous structure could not only increase the exposure of active sites, but also contribute to fast mass transfer. High-resolution TEM (HRTEM) is adopted to investigate the detailed structure of the N-Ni₅P₄ @CoP/CFP. As shown in Fig. 1g, an obvious lattice boundary marked with red dashed line can be observed, indicating that the tightly integrated heterointerface is successfully constructed for the N-Ni₅P₄ @CoP/CFP. By carefully matching the lattice fringes of both sides of interface (Fig. 1g, h), the fringe spacings of 2.46 and 1.89 Å can be correlated to the (111) and (211) planes of CoP (Fig. 1i) and the interplanar spacings of 1.91 and 2.23 Å can be matched with (213) and (210) planes of Ni₅P₄ (Fig. 1j), which can be further confirmed by the related fast Fourier transformation (FFT) pattern. The energy dispersive X-ray spectroscopy (EDS) elemental mapping images indicate the presence of

Co, Ni, P and N elements in the N-Ni₅P₄ @CoP/CFP (Fig. 1k and Fig. S5). The signal of P atoms can be clearly detected throughout the whole N-Ni₅P₄/CoP nanowire. The Co element is observed to be concentrated into the inner region, whereas the Ni and N elements are distributed on the outer dendritic layer, suggesting that the N is doped in the Ni₅P₄ component. Additionally, the similar approach is adopted to prepare the pure N-Ni₅P₄ and CoP on CFP (denoted as N-Ni₅P₄/CFP and CoP/CFP) for comparison (Fig. S6).

The X-ray photoelectron spectroscopy (XPS) is performed to investigate the chemical composition and valence state of the N-Ni₅P₄/CFP, CoP/CFP and N-Ni₅P₄ @CoP/CFP. The wide-scanning XPS spectrum (Fig. S7) shows the existence of Ni, Co, N and P in the N-Ni₅P₄ @CoP/CFP, which is entirely consistent with the result of EDS elemental mapping. Fine-scanning Ni 2p spectrum of the N-Ni₅P₄ @CoP/CFP (Fig. 2a) displays that two typical peaks at 852.7 and 870.1 eV correspond to Ni-P bonds, suggesting the formation of nickel phosphide species [29]. The peaks located at 855.4 and 873.1 eV can be assigned to Ni-O species, which may be caused by the inevitable surface oxidation in air [30]. Fig. S8a presents the N 1s spectrum of the N-Ni₅P₄ @CoP/CFP, in which the peak at 398.7 eV belongs to Ni-N bonds and another peak at 400.3 eV corresponds to C-N bonds [31,32]. It can also be seen that the Ni-N peak for the N-Ni₅P₄ @CoP/CFP exhibits a positive shift of 0.5 eV in comparison with the N-Ni₅P₄/CFP, indicating the electronic interaction in the N-Ni₅P₄ @CoP heterogeneous interface [4]. The Co 2p spectrum of N-Ni₅P₄ @CoP/CFP in Fig. 2b shows the peaks at 779 and 794.1 eV assigned to Co-P bonds, confirming the successful formation of the cobalt phosphide [33]. The peaks centered at the binding energy of 782.1 and 798.4 eV belong to Co-O species. For the P 2p spectrum of N-Ni₅P₄ @CoP/CFP (Fig. S8b), two peaks at 128.8 and 129.7 eV are attributed to the metal-P bond, and the broad peak at 133.7 eV is ascribed to the P-O species [34,35]. Besides, the peak area of metal-P bonds for N-Ni₅P₄ @CoP/CFP is signally higher than that for N-Ni₅P₄/CFP and CoP/CFP, suggesting that more phosphide species are exposed for the N-Ni₅P₄ @CoP/CFP. It is worth noting that the binding energy of Co-P for N-Ni₅P₄ @CoP/CFP exhibits a positive shift compared to that for CoP/CFP, confirming the electrons transfer from CoP to N-Ni₅P₄ at the heterogeneous interface [2]. There is no obvious shift of Ni-P peaks in N-Ni₅P₄ @CoP/CFP relative to N-Ni₅P₄/CFP can be observed, demonstrating that the transferred electrons may be concentrated on the P atoms to form the electron-rich P sites in N-Ni₅P₄ @CoP/CFP. Furthermore, the obvious Ni-N peak shift can be observed for the N-Ni₅P₄ @CoP/CFP and N-Ni₅P₄/CFP in Raman spectra, which can also prove the presence of the electronic reciprocity between N-Ni₅P₄ and CoP at the interface (Fig. S9) [36,37]. Such an interfacial charge redistribution could be beneficial to promoting the formation of electron-rich N-Ni₅P₄ region [38], and the electron-deficient CoP region [39], which are evidenced by work function (Φ) difference between CoP/CFP (4.66 eV) and N-Ni₅P₄/CFP (4.92 eV) in Fig. S10 using ultraviolet photoelectron spectroscopy (UPS).

X-ray absorption near-edge structure (XANES) and extended X-ray absorption fine structure (EXAFS) spectra are recorded to investigate the local coordination environments of N-Ni₅P₄ @CoP/CFP, together with the Co foil, CoO, CoP, Ni foil, NiP and Ni₃N as the comparison. The Co K-edge XANES spectrum shows that the Co absorption-edge for the N-Ni₅P₄ @CoP/CFP shifts to the higher energy compared with that for CoP (Fig. 2c and Fig. S11), indicating that the electron density around the Co atom can be reduced upon the formation of N-Ni₅P₄ @CoP interface [40], which is in accordance with Co 2p XPS results. Furthermore, the binding energy of Co atoms for the N-Ni₅P₄ @CoP/CFP is lower than that for the control CoO, but higher than that for the Co foil, implying that the average oxidation state of cobalt is between 0 and +2 for the N-Ni₅P₄ @CoP/CFP [41]. With respect to Co K-edge Fourier transform EXAFS (FT-EXAFS) spectrum in K space (Fig. S12), the coordination peaks for the N-Ni₅P₄ @CoP/CFP show a similar oscillation trend but relatively strong intensity compared to that of reference CoP. The results suggest that the Co atom in the N-Ni₅P₄ @CoP/CFP has the similar

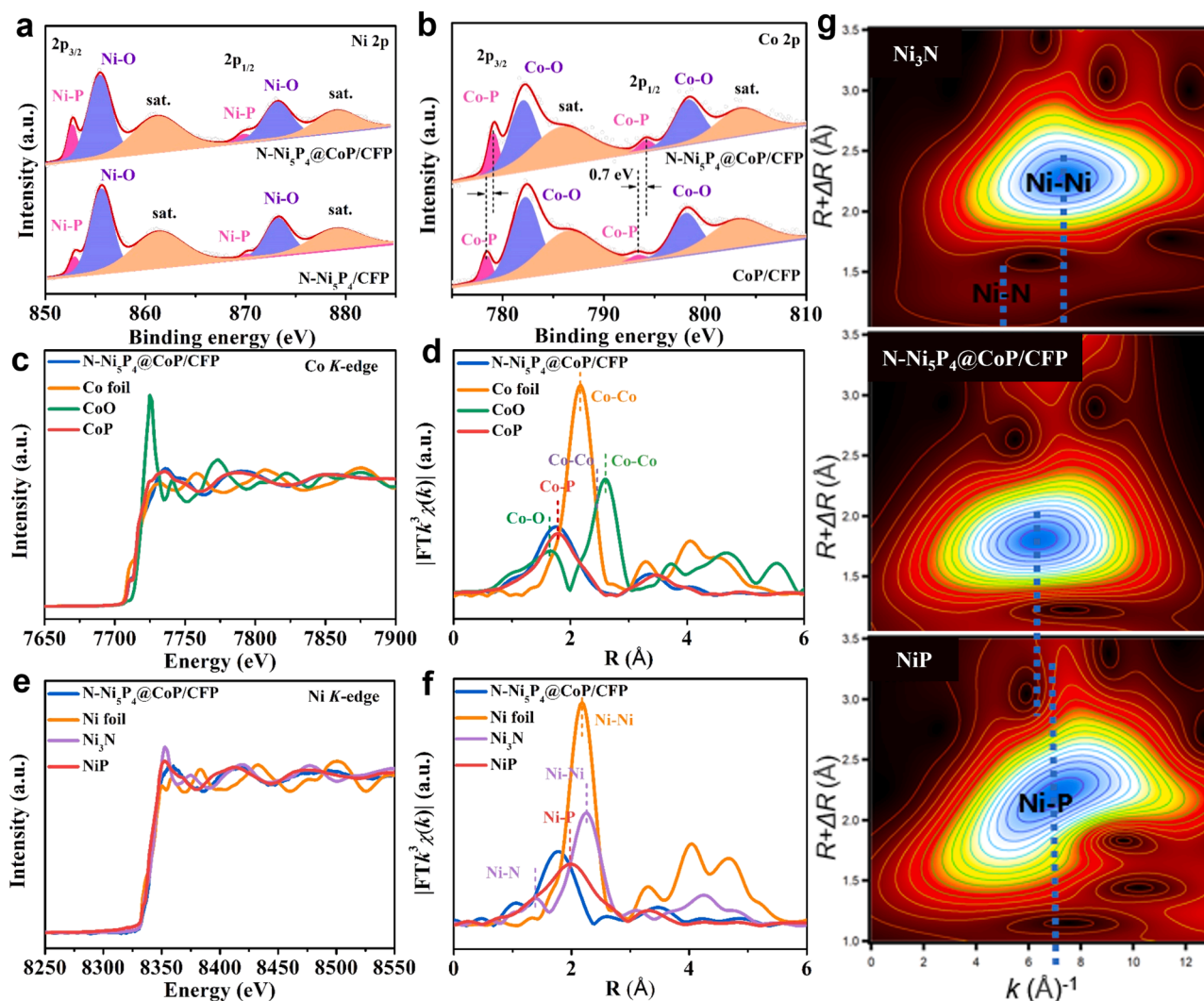


Fig. 2. Fine-scanning XPS spectra of (a) Ni 2p, (b) Co 2p for CoP/CFP, N-Ni₅P₄/CFP and N-Ni₅P₄@CoP/CFP. (c) Co K-edge XANES spectra, and (b) Co K-edge FT-EXAFS spectra of the N-Ni₅P₄@CoP/CFP, CoO, CoP and Co foil. (e) Ni K-edge XANES spectra, and (f) Ni K-edge FT-EXAFS spectra of the N-Ni₅P₄@CoP/CFP, Ni₃N, NiP, and Ni foil. (g) Wavelet transform for the k^3 -weighted EXAFS signals of Ni for N-Ni₅P₄@CoP/CFP, Ni₃N, and NiP.

coordination structure as that of CoP, while the former possess higher coordination number [42]. As seen from the Co K-edge FT-EXAFS spectrum in R space (Fig. 2d), the dominant peak at 1.79 Å for the CoP can be ascribed to the Co-P coordination. Notably, the Co-P peak for the N-Ni₅P₄@CoP/CFP exhibits a negative shift compared to that for the reference CoP (Fig. S13), which may be ascribed to the decrease of electron density around Co atoms [43]. The above analysis shows that the electron-deficient Co atoms are generated in the N-Ni₅P₄@CoP/CFP, which could act as the electrophilic centers to readily adsorb N₂H₄* in catalytic HzOR process. For the Ni K-edge XANES spectrum, the absorption edge of N-Ni₅P₄@CoP/CFP slightly shifts to high energy compared to that of NiP, indicating the average valence of Ni is increased (Fig. 2e and Fig. S14) [44]. The Ni K-edge FT-EXAFS spectrum in K space declares that the oscillation trend of N-Ni₅P₄@CoP/CFP is close to those of Ni₃N and NiP but completely different to that of Ni foil (Fig. S15), manifesting that the coordination structure of Ni atoms involves the Ni-P and Ni-N bonds for the N-Ni₅P₄@CoP/CFP. We further perform FT-EXAFS fitting to acquire more information about the Ni coordination environment for the N-Ni₅P₄@CoP/CFP (Fig. 2f). It is worth noting that the Ni-P peak for N-Ni₅P₄@CoP/CFP (1.76 Å) becomes slightly broader than that for the NiP (1.98 Å), further suggesting the formation of Ni-N bonds in the N-Ni₅P₄@CoP/CFP [45]. Meanwhile, the negative shift of the Ni-P peak attributes to that the electronic

structure of Ni atoms is changed by the formed Ni-N coordination [46]. In order to further distinguish the Ni-N and Ni-P bonds, the wavelet transform (WT) is also executed to detect the coordination environment of the Ni atom (Fig. 2g). Two WT maximum values are identified to be at 5.1 and 7.2 Å⁻¹ for the Ni₃N, which correspond to the Ni-N and Ni-Ni bonds, respectively. The maximum intensity of NiP is located at 7.0 Å⁻¹, which is attributed to the Ni-P bond. The N-Ni₅P₄@CoP/CFP shows a maximum intensity at 6.4 Å⁻¹, which is close to the NiP (7.0 Å⁻¹), indicating that Ni-P coordination mode is predominated for the N-Ni₅P₄@CoP/CFP [47]. The slightly negative shift of the maximum intensity can be observed for the N-Ni₅P₄@CoP/CFP compared to that for the NiP, which is caused by the atomic number difference between P and N [31], indicating the formation of the N-Ni and Ni-P coordination after the substitution of N for partial P.

3.2. Theoretical calculations

Density functional theory (DFT) calculation is employed to deeply investigate the relationship between electronic structure and catalytic activity, in which the structural models of CoP, Ni₅P₄, N-Ni₅P₄, and N-Ni₅P₄@CoP heterostructure are deliberately simulated (Fig. 3a and Fig. S16). The Φ is first calculated to be 3.80, 3.83, and 3.86 eV for the CoP, Ni₅P₄, and N-Ni₅P₄, respectively (Fig. S17). Notably, the difference

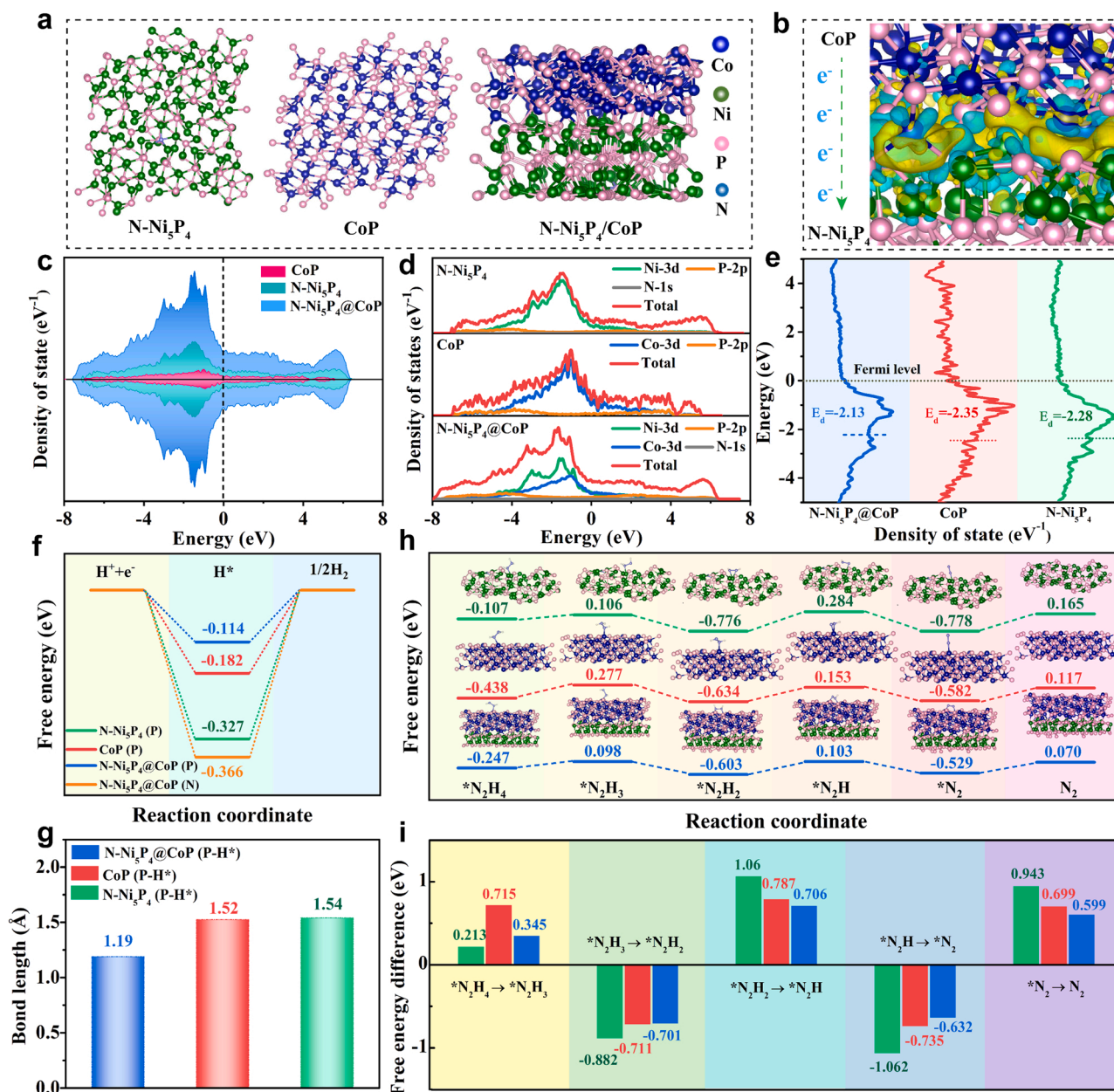


Fig. 3. (a) Structural models of the N-Ni₅P₄, CoP and N-Ni₅P₄@CoP. (b) Charge density difference of the N-Ni₅P₄@CoP. (c) DOS, and (d, e) PDOS of the CoP, N-Ni₅P₄, and N-Ni₅P₄@CoP. (f) Gibbs free energy diagram of the ΔG_{H^*} , and (g) P-H* bond length for the CoP, N-Ni₅P₄, and N-Ni₅P₄@CoP. (h) Reaction pathways in the HzOR process, and (i) Corresponding free energy difference for the N-Ni₅P₄, CoP and N-Ni₅P₄@CoP.

of work function ($\Delta\Phi$) between CoP and N-Ni₅P₄ is larger than that between CoP and Ni₅P₄, which indicates that the N incorporation can tailor the energy level structure for generating a more powerful interfacial electronic field, thus promoting the charge transfer from CoP to N-Ni₅P₄ at the heterointerface [48]. To deeply reveal the effect of N incorporation at the atomic level, the bond length of Ni-P bond that share the same Ni atom with and without a Ni-N bond are calculated (Fig. S18), in which the former is observed to be slightly longer than the latter. The result indicates that formation of Ni-N bonds in the N-Ni₅P₄@CoP could increase the length of neighbor Ni-P bonds, thus adjusting the atomic interaction between Ni and P to regulate the interfacial electronic structure [20]. As a proof of concept, the charge density difference is then determined for the N-Ni₅P₄@CoP heterostructure, as shown in Fig. 3b. The charge redistribution takes place at the heterointerface, where the electron-rich N-Ni₅P₄ area (marked with yellow colors) and electron-deficient CoP area (marked with cyan colors) can be

clearly distinguished, in agreement with above the XPS results. The nucleophilic N-Ni₅P₄ area with electron accumulation could optimize the absorption energy of hydrogen intermediates for facilitating HER, whereas the electrophilic CoP area with electron deficiency may promote the absorption process of N₂H₄* for promoting HzOR.

The density of states (DOS) is calculated to further explore the change of electronic structure after the formation of interface between N-Ni₅P₄ and CoP (Fig. 3c) [49]. As can be seen, the local density of states for the N-Ni₅P₄, CoP, and N-Ni₅P₄@CoP heterostructure reside across the Fermi level, which indicates their metallic feature [50]. Notably, the N-Ni₅P₄@CoP heterostructure exhibits more occupation at Fermi level than that of N-Ni₅P₄ and CoP, suggesting that the formation of heterointerface leads to higher conductivity for facilitating the charge transfer capability during electrochemical reaction process [41]. The comparison among N-Ni₅P₄, CoP, and N-Ni₅P₄@CoP in the projected density of states (PDOS) diagram manifests that the hybridization between Co 3d

and Ni 3d orbitals makes contribution to the total DOS of N-Ni₅P₄ @CoP near the Fermi level (Fig. 3d) [51]. Such 3d-orbitals hybridization could endow the coupling interface with strong electronic interaction [52], which would provide numerous charge transfer channels to shorten the electronic migration path. The d-band center (E_d) is used as the descriptor to investigate the binding strength of reaction intermediates on the N-Ni₅P₄ @CoP surface [53,54]. As displayed in Fig. 3e, the E_d of the N-Ni₅P₄ @CoP (−2.13 eV) is closer to the Fermi level compared with those of the CoP (−2.35 eV) and N-Ni₅P₄ (−2.28 eV), illustrating that the active sites on the N-Ni₅P₄ @CoP surface has the stronger adsorption for reaction intermediates.

The catalytic pathways of N-Ni₅P₄, CoP, and N-Ni₅P₄ @CoP are further studied to understand the kinetic energy barriers for the HER and HzOR process. It is generally accepted that the thermoneutral Gibbs free energy of hydrogen intermediate absorption ($\Delta G_{H^*} \approx 0$) on the active sites is beneficial for boosting HER performance, which could balance

the hydrogen adsorption/desorption processes for enhancing reaction kinetics [55]. As shown in the free energy diagram (Fig. 3f), the ΔG_{H^*} of P sites in N-Ni₅P₄ area (−0.114 eV) for N-Ni₅P₄ @CoP is much closer to zero than that of N sites in the same area (−0.366 eV), which indicates P sites are more active than N sites for H⁺ adsorption in HER process. Furthermore, the contrast for ΔG_{H^*} of P sites among N-Ni₅P₄, CoP, and N-Ni₅P₄ @CoP reveals that the N-Ni₅P₄ @CoP possess more favorable H⁺ adsorption kinetics toward the HER. Fig. S19 exhibits the H⁺ adsorption on the N-Ni₅P₄, CoP and N-Ni₅P₄ @CoP models, in which the bond length between P sites and H⁺ (P-H⁺) for the N-Ni₅P₄, CoP, N-Ni₅P₄ @CoP is determined to be 1.54, 1.52, and 1.19 Å, respectively. The shortest P-H⁺ bond length in the N-Ni₅P₄ @CoP represents the strongest binding strength of H⁺, which could facilitate the adsorption of hydrogen intermediates on the catalyst surface (Fig. 3g) [56], thus improving intrinsic HER catalytic activity. Fig. 3h shows the Gibbs free energy diagrams of typical HzOR processes for the N-Ni₅P₄, CoP,

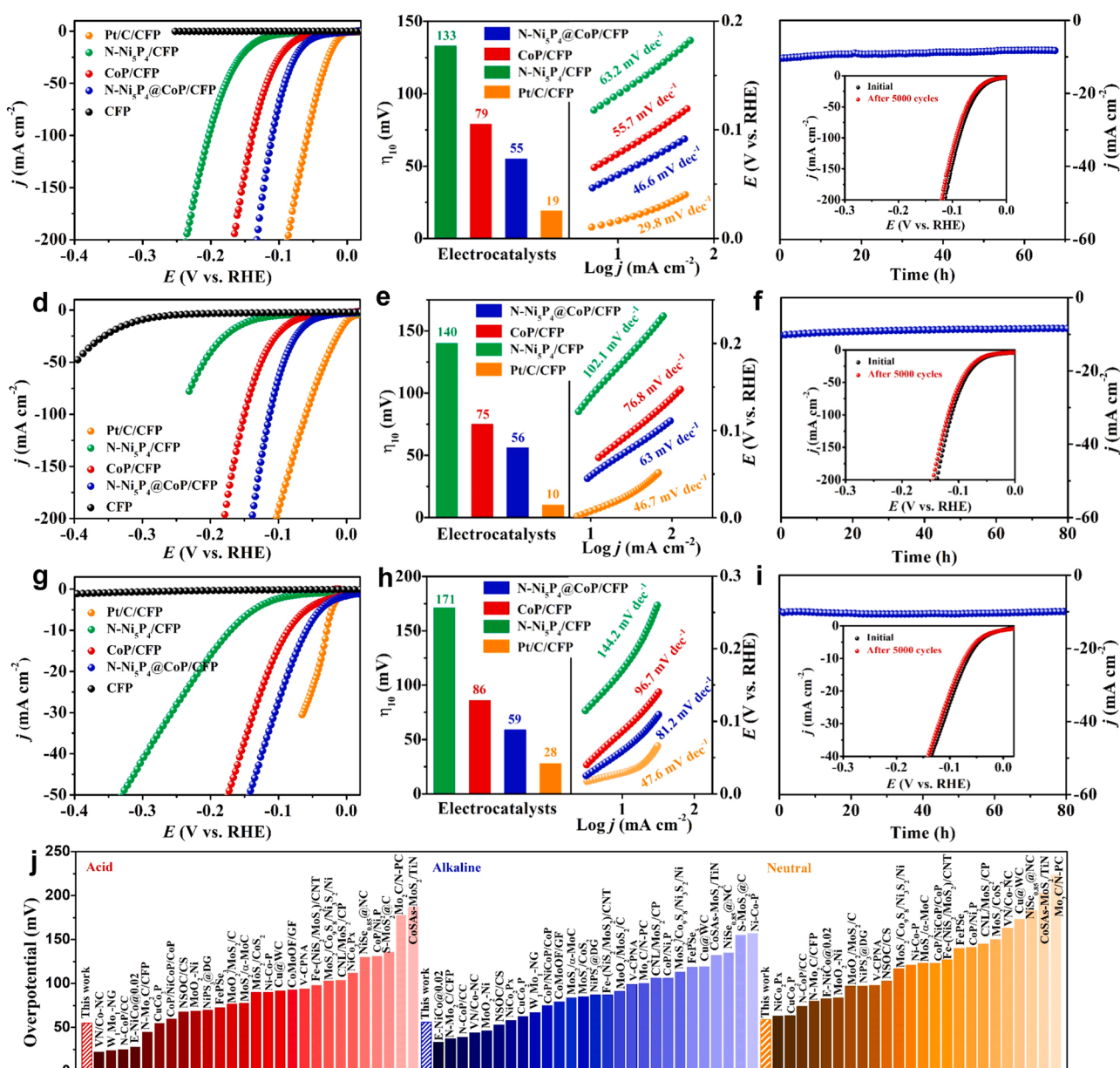


Fig. 4. LSV curves of the N-Ni₅P₄ @CoP/CFP and contrastive catalysts in (a) 0.5 M H₂SO₄, (d) 1.0 M KOH, and (g) 1.0 M PBS solutions. η_{10} and Tafel plots for above catalysts in (b) 0.5 M H₂SO₄, (e) 1.0 M KOH and (h) 1.0 M PBS solutions. Chronoamperometric curves and LSV curves of the N-Ni₅P₄ @CoP/CFP before and after 5000 cycles in (c) 0.5 M H₂SO₄, (f) 1.0 M KOH and (i) 1.0 M PBS solutions. (j) Comparison of the HER overpotential at 10 mA cm⁻² for the N-Ni₅P₄ @CoP/CFP with recently reported catalysts.

N-Ni₅P₄ @CoP, which involve the adsorption of hydrazine molecule and four consecutive dehydrogenation steps (N₂H₄ → N₂H₃ → N₂H₂ → N₂H → N₂). It should be noted that the N₂H₄ adsorption on Co sites of the N-Ni₅P₄ @CoP is exothermic (0.247 eV), lower than that on Ni sites of the N-Ni₅P₄ surface (0.107 eV) but higher than that on Co sites of the CoP (0.438 eV), indicating that the adsorption of N₂H₄ is not too strong or too weak on the N-Ni₅P₄ @CoP surface. Such moderate binding strength for N₂H₄ molecules on the surface may facilitate the subsequent dehydrogenation steps [57]. It can also be seen that the rate-determining step (RDS) is the dehydrogenation from *N₂H₂ to *N₂H for N-Ni₅P₄, CoP, and N-Ni₅P₄ @CoP (Fig. 3i), in which the free energy difference for N-Ni₅P₄ @CoP (0.706 eV) is lower than that of N-Ni₅P₄ (1.06 eV) and CoP (0.787 eV). Based on the above analysis, dual sites are formed on the N-Ni₅P₄ @CoP heterointerface, where the nucleophilic P sites in the N-Ni₅P₄ region can optimize the adsorption energy of H* and electrophilic Co sites in the CoP region can promote the dehydrogenation kinetics of N₂H₄*, thus being expected to realize the outstanding catalytic activity for HER and HzOR synchronously.

3.3. Electrocatalytic HER performance

The HER performance of N-Ni₅P₄ @CoP/CFP in the whole pH range (0.5 M H₂SO₄, 1.0 M KOH and 1.0 M PBS electrolytes) is evaluated by the iR-corrected linear sweep voltammetry (LSV) with a standard three-electrode system, and the N-Ni₅P₄/CFP, CoP/CFP, bare CFP and commercial Pt/C catalyst loaded on CFP substrate (Pt/C/CFP) are also measured as controls. The N-Ni₅P₄ @CoP/CFP exhibits a remarkable HER activity in 0.5 M H₂SO₄ solution (Fig. 4a), in which the cathodic current density rises rapidly along the increase of applied potential and a small overpotential (η_{10} = 55 mV) is required to obtain a current density of 10 mA cm⁻² (Fig. 4b, left), surpassing those of the N-Ni₅P₄/CFP (η_{10} = 133 mV) and CoP/CFP (η_{10} = 79 mV). Except for the acidic electrolyte, the N-Ni₅P₄ @CoP/CFP can also achieve excellent HER activity in the alkaline and neutral solution, which are of significance in some practical applications such as water-splitting electrolyzer, seawater electrolysis system, and microbial electrolysis cells [27]. As shown in Fig. 4e (left), the N-Ni₅P₄ @CoP/CFP presents an overpotential of merely 56 mV for achieving 10 mA cm⁻² in alkaline media, lower than that of the N-Ni₅P₄/CFP (η_{10} = 140 mV) and CoP/CFP (η_{10} = 75 mV). For the N-Ni₅P₄ @CoP/CFP, the HER overpotential is recorded as 59 mV at 10 mA cm⁻² in neutral electrolyte, which is lower than those of the N-Ni₅P₄/CFP (η_{10} = 171 mV) and CoP/CFP (η_{10} = 86 mV), although higher than that of the Pt/C/CFP (η_{10} = 28 mV). Apparently, the N-Ni₅P₄ @CoP/CFP displays the attractive HER activities in acid, alkaline and neutral surroundings, which are also superior to the majority of the recently reported non-noble metal catalysts (Fig. 4j and Table S1). The excellent catalytic activity is closely related to the accelerated reaction kinetics, for which the Tafel slope is a significant evaluation parameter. The corresponding Tafel slopes of N-Ni₅P₄ @CoP/CFP are estimated to 46.6, 63.0, and 81.2 mV dec⁻¹ in 0.5 M H₂SO₄, 1.0 M KOH, and 1.0 M PBS, respectively, which are much lower than those of the N-Ni₅P₄/CFP (63.2, 102.1, and 144.2 mV dec⁻¹) and CoP/CFP (55.7, 76.8, and 96.7 mV dec⁻¹), and even close to that of the Pt/C/CFP (29.8, 46.7, and 49 mV dec⁻¹), suggesting the superb HER kinetics for the N-Ni₅P₄ @CoP/CFP (right of Fig. 4b, 4e and 4 h). The electrochemical active surface area (ECSA), which can be estimated by measuring double-layer capacitance (C_{dl}), is usually employed to shed light on the origin of the improved HER activity. As illustrated in Fig. S20–22, the C_{dl} values of the N-Ni₅P₄ @CoP/CFP are found to be 134.2, 106.0, and 76.0 mF cm⁻² in 0.5 M H₂SO₄, 1.0 M KOH and 1.0 M PBS, respectively, which are higher than those of the N-Ni₅P₄/CFP and CoP/CFP. The higher C_{dl} value means more exposed active sites for the N-Ni₅P₄ @CoP. It is obvious that the ECSA-normalized current density of the N-Ni₅P₄ @CoP/CFP is also larger than that of the N-Ni₅P₄/CFP and CoP/CFP under the same overpotential, suggesting the high intrinsic HER activities for the N-Ni₅P₄ @CoP/CFP in all the pH range (Fig. S23), which is consistent to

the DFT results. The fitting plots of electrochemical impedance spectroscopy (EIS) of the N-Ni₅P₄ @CoP/CFP shows a smaller complete semicircle relative to the N-Ni₅P₄/CFP and CoP/CFP in all the pH range, reflecting a faster charge transfer during HER process (Fig. S24). Long-term stability is an important criterion to evaluate the practical value for catalysts, especially for catalysts operated in different application scenarios. As shown in the chronoamperometric curves for N-Ni₅P₄ @CoP/CFP (Figs. 4c, 4f and 4i), the current density exhibits negligible decay over 50 h in 0.5 M H₂SO₄, 1.0 M KOH and 1.0 M PBS electrolytes, demonstrating the excellent HER stability. Additionally, the superior cycling durability for N-Ni₅P₄ @CoP/CFP can be manifested by linear sweep voltammetry measurement (inset of Figs. 4c, 4f and 4i), in which the polarization curves hardly changes before and after 5000 voltammetry cycles in 0.5 M H₂SO₄, 1.0 M KOH and 1.0 M PBS. Seawater is considered as an abundant hydrogen source, for which it is meaningful to assess HER performance for the N-Ni₅P₄ @CoP/CFP in real seawater. Notably, the N-Ni₅P₄ @CoP/CFP exhibits the lower overpotential (η_{10} = 250 mV) and Tafel slope (179.6 mV dec⁻¹), smaller charge-transfer resistances (R_{ct} = 36 Ω), and the higher active surface area (C_{dl} = 48 mF cm⁻²) compared to the control CoP/CFP and N-Ni₅P₄/CFP, illustrating the excellent catalytic HER activity for N-Ni₅P₄ @CoP/CFP in real seawater (Fig. S25).

3.4. Electrocatalytic HzOR performance

The electrocatalytic HzOR performance is measured for the investigated different catalysts in 0.1 M N₂H₄/1.0 M KOH solution. Fig. 5a displays the iR-corrected LSV curves for the N-Ni₅P₄ @CoP/CFP, N-Ni₅P₄/CFP, CoP/CFP, and Pt/C/CFP, intuitively indicating much better catalytic activity for the N-Ni₅P₄ @CoP/CFP compared with the counterparts. Specifically, the N-Ni₅P₄ @CoP/CFP only requires an ultralow potential of −32 mV to achieve anodic current density of 10 mA cm⁻², which is far more excellent than those of the N-Ni₅P₄/CFP (50 mV), CoP/CFP (−21 mV), Pt/C/CFP (154 mV), and also surpass most of the recently reported non-noble catalysts (Fig. 5b and Table S2). Additionally, the corresponding Tafel slope of the N-Ni₅P₄ @CoP/CFP is calculated to be 24.9 mV dec⁻¹, lower than those of CoP/CFP (41.5 mV dec⁻¹), N-Ni₅P₄/CFP (60.4 mV dec⁻¹) and Pt/C/CFP (96.9 mV dec⁻¹), which suggests the most favorable kinetics toward HzOR for the N-Ni₅P₄ @CoP/CFP (Fig. 5c). Moreover, EIS result shows that the N-Ni₅P₄ @CoP/CFP possesses the lower charge transfer resistance (R_{ct}) than those of the N-Ni₅P₄/CFP and CoP/CFP, illustrating the faster charge transport process during HzOR for the N-Ni₅P₄ @CoP/CFP (Fig. 5d). The chronoamperometric test shows the excellent long-term durability toward HzOR for the N-Ni₅P₄ @CoP/CFP (Fig. 5e). Fig. 5 f shows the comparison of LSV curves toward HzOR and OER for the N-Ni₅P₄ @CoP/CFP. It only requires the HzOR potentials of −32, −22, −8, and 60 mV to reach the current densities of 10, 20, 50, and 100 mA cm⁻², respectively, whereas much higher OER potentials of 1504, 1515, 1534, and 1553 mV are needed, demonstrating the great HzOR kinetic advantages [4]. The corresponding Tafel slopes and EIS results also illustrate the more favorable reaction kinetics and charge transfer for HzOR than OER under the same potential (Fig. 5 g and Fig. S26). Such boosted kinetics enable N₂H₄* rather than OH* to be more easily absorbed on the N-Ni₅P₄ @CoP/CFP, and thus the absorbed N₂H₄* could undergo a rapid dehydrogenation process.

To obtain the information on the charge transfer kinetics in a wide potential window, EIS is performed at the potential range from −0.1 to 0.1 V for the N-Ni₅P₄/CFP, CoP/CFP and N-Ni₅P₄ @CoP/CFP (Fig. 5 h, and Fig. S27). In the Nyquist plot of the CoP/CFP, the semicircles first become smaller and then larger with the potential increase from −0.1 to 0.1 V, suggesting that the lower charge transfer under high potential range. For the N-Ni₅P₄/CFP, Nyquist plot shows approximated vertical lines from −0.1 V to −0.05 V, which manifests the high charge transfer resistance and the inferior electrical conductivity under the low potential range. Interestingly, the N-Ni₅P₄ @CoP/CFP exhibits the gradually

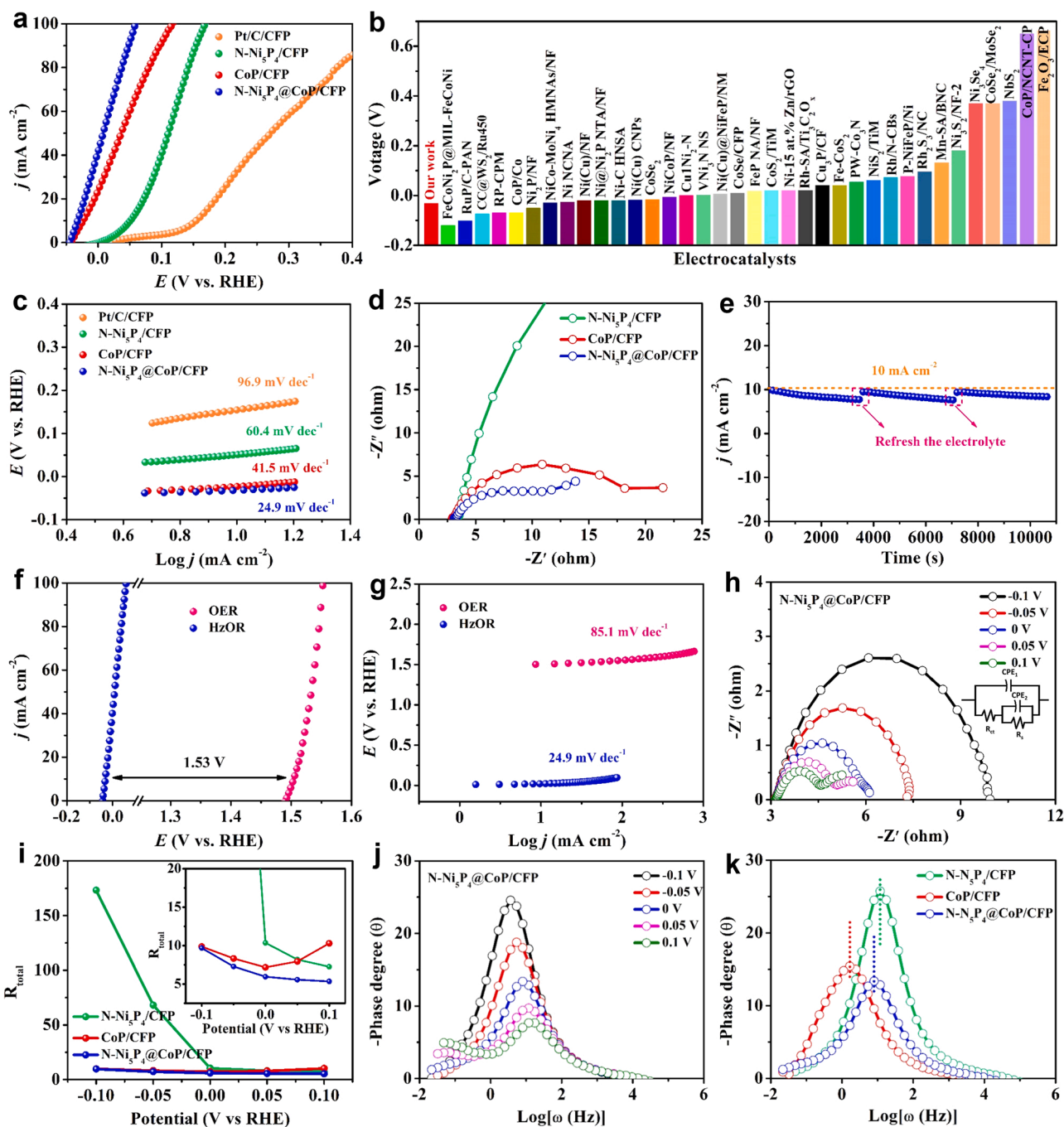


Fig. 5. (a) iR-corrected LSV curves of the N-Ni₅P₄@CoP/CFP and contrastive catalysts. (b) Comparison of the HzOR overpotential at 10 mA cm⁻² for the N-Ni₅P₄@CoP/CFP with recently reported catalysts. (c) Tafel plots, and (d) Nyquist plots of above catalysts. (e) The chronoamperometric curve at 10 mA cm⁻² for the N-Ni₅P₄@CoP/CFP. (f) LSV curves, and (g) Tafel slope of the N-Ni₅P₄@CoP/CFP for HzOR and OER. (h) Nyquist plots under different potentials of N-Ni₅P₄@CoP/CFP. (i) Calculated R_{total} under different potentials for the N-Ni₅P₄@CoP/CFP and and control catalysts. (j) Bode phase plots under different potentials for the N-Ni₅P₄@CoP/CFP. (k) Bode phase plots at 0 V for the N-Ni₅P₄@CoP/CFP and contrastive catalysts.

diminishing semicircles with the potential increase that can supply more electrons, indicating the fast charge transfer under all applied potentials. In order to more intuitively show the charge transfer kinetic differences of above catalysts at each potentials, the values of total resistance (R_{total}) are determined by calculating the values of charge transfer resistance (R_{ct}) and solution resistance (R_s) in a potential range from -0.1 to 0.1 V (Table S3) [58]. It can be seen that the R_{total} for the N-Ni₅P₄@CoP/CFP decreases gradually as the potential increases and maintains the lower value at each applied potential compared to contrast catalysts, suggesting that the N-Ni₅P₄@CoP/CFP has the faster charge transfer

kinetics in a wide potential window (Fig. 5i), which is in good agreement with the DOS results [59]. The corresponding Bode phase plots show that the peak of the N-Ni₅P₄@CoP/CFP gradually decreases and shifts to high frequency with the increased potential, whereas the CoP/CFP and N-Ni₅P₄/CFP show the different trends (Fig. 5j and Fig. S28). These results suggest that the N-Ni₅P₄@CoP/CFP possesses the enhanced charge transfer and improved reaction kinetics, which could be beneficial to improving the conductivity of catalysts and reducing the extra energy loss in practical case. Additionally, the comparison of peaks at 0 V for the N-Ni₅P₄@CoP/CFP, CoP/CFP and N-Ni₅P₄/CFP are shown in

Fig. 5k. Relative to N-Ni₅P₄/CFP, the phase peak of the N-Ni₅P₄@CoP/CFP shows a lower phase angle and moves towards the lower frequency, which represents that more N₂H₄ is adsorbed on the surface of the N-Ni₅P₄@CoP/CFP during HzOR process, suggesting the favorable adsorption ability for N₂H₄ molecules [23]. The peak of the N-Ni₅P₄@CoP/CFP decreases and moves towards the higher frequency compared to CoP/CFP, demonstrating the faster charge transfer kinetics [60]. The N-Ni₅P₄@CoP/CFP with optimized adsorption kinetics and the enhanced charge transfer might moderate the binding strength for N₂H₄ molecules on the surface, and thus facilitate the subsequent multi-step dehydrogenation process, which is in line with the DFT results.

3.5. Electrocatalytic OHzS performance

Encouraged by the superior catalytic performance toward both HER and HzOR for the N-Ni₅P₄@CoP/CFP, a two-electrode OHzS electrolyzer is assembled by serving the bifunctional N-Ni₅P₄@CoP/CFP as the anode and the cathode in 1.0 M KOH/0.1 M N₂H₄ electrolyte. As shown in Figs. 6a and 6b, the OHzS electrolyzer driven by N-Ni₅P₄@CoP/CFP only need the small cell voltages of 0.037, 0.069, 0.165, and 0.317 V to reach the current densities of 10, 20, 50, and 100 mA cm⁻², respectively, which lower than those of OWS electrolyzer at the same current densities, illustrating a significant enhancement for the energy efficiency in the hydrazine-assisted hydrogen production [11]. As can be

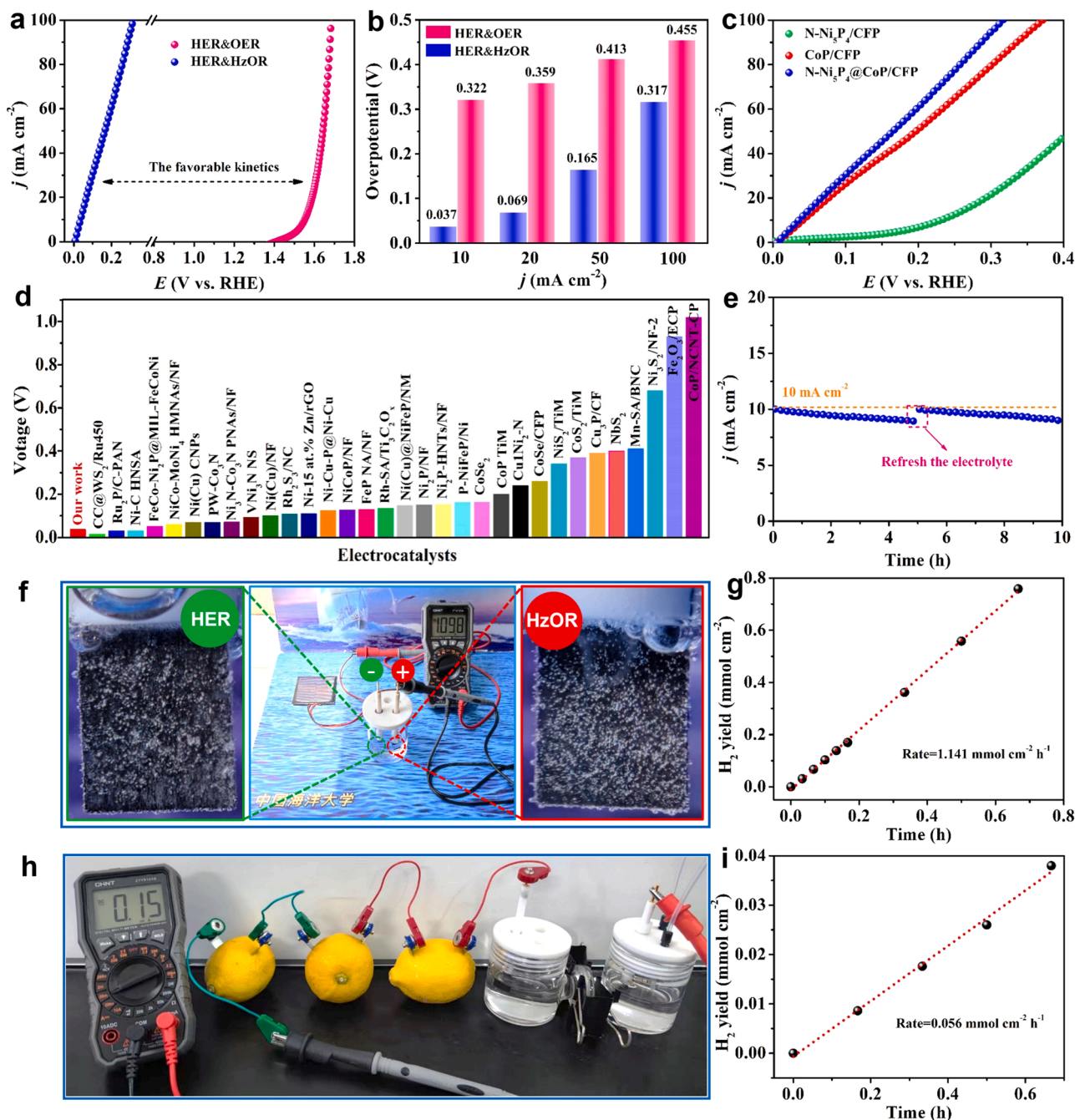


Fig. 6. (a) LSV curves, and (b) overpotentials at different current densities of the N-Ni₅P₄@CoP/CFP for OHzS and OWS electrolyzers. (c) LSV curves of the OHzS electrolyzer based on N-Ni₅P₄@CoP/CFP and contrastive catalysts. (d) Comparison of cell voltages at 10 mA cm⁻² for the OHzS systems based on N-Ni₅P₄@CoP/CFP and recently reported catalysts. (e) The chronoamperometric curve of OHzS electrolyzer based on N-Ni₅P₄@CoP/CFP. Digital photograph of the OHzS electrolyzer powered by (f) Commercial solar cell, and (h) lemon battery. (g, i) Corresponding H₂ production rate.

seen in Fig. 6c, the cell voltage at 10 mA cm^{-2} for the $\text{N-Ni}_5\text{P}_4$ @CoP/CFP based OHZS electrolyzer is considerably lower than those of the counterparts based on $\text{N-Ni}_5\text{P}_4$ /CFP (0.231 V), CoP/CFP (0.041 V), and also superior to those of recently reported OHZS electrolyzers assembled by bifunctional catalysts (Fig. 6d and Table S4). More importantly, the OHZS electrolyzer assembled by $\text{N-Ni}_5\text{P}_4$ @CoP/CFP shows outstanding long-term durability after continuous electrolysis over 10000 s (Fig. 6e). The SEM and XRD analysis (Fig. S29 and S30) display that there are no obvious changes in structure after long-term HER and HzOR stability test, further confirming the wonderful durability of the $\text{N-Ni}_5\text{P}_4$ @CoP/CFP. In order to evaluate the potential of practical application, the OHZS electrolyzer is paired with a commercial Si solar cell (1.0 V, 0.5 A) to drive OHZS electrolysis in real sunlight (Fig. 6 f), in which the obvious gas bubble release can be observed and a promising H_2 production rate of $1.141 \text{ mmol cm}^{-2} \text{ h}^{-1}$ can be achieved (Fig. 6 g). Interestingly, a home-made lemon battery with an open-circuit voltage of 0.05 V can deliver a H_2 production rate of $0.056 \text{ mmol cm}^{-2} \text{ h}^{-1}$ in 1.0 M KOH/0.1 M N_2H_4 (Fig. 6 h and 6i). Such obtained ultra-low operating voltage may be resulted from the synergistic effect of accelerated mass transport, the fast electron transfer, and the boosted intrinsic activity. These results reveal that the as-prepared $\text{N-Ni}_5\text{P}_4$ @CoP/CFP has potential applications in for hydrazine-assisted energy-saving H_2 production.

3.6. The proposed HER and HzOR mechanism

The radar charts, which display the comparison for the potentials of HzOR, OHZS and HER at 10 mA cm^{-2} of current density, are applied to systematically assess the comprehensive performance of the above

investigated catalysts. As shown in Fig. 7a, the larger area of closed loop means the better comprehensive catalytic performance. Obviously, the $\text{N-Ni}_5\text{P}_4$ @CoP/CFP exhibits the excellent catalytic performance, which outperforms the contrastive CoP/CFP and $\text{N-Ni}_5\text{P}_4$ /CFP. The possible reason of wonderful HER and HzOR activities for the $\text{N-Ni}_5\text{P}_4$ @CoP/CFP are as follows (Fig. 7b). A heterogenous nanowire array consisting of abundant $\text{N-Ni}_5\text{P}_4$ @CoP interface has been obtained on carbon fiber paper, in which an adjustable Ni coordination structure can fine-regulate the energy level structure of $\text{N-Ni}_5\text{P}_4$ to enhance interfacial electric field for facilitating charge transfer from CoP to $\text{N-Ni}_5\text{P}_4$. Such an elaborately modulated charge redistribution can benefit to the formation of well-defined electrophilic Co sites and nucleophilic P sites in the CoP and in $\text{N-Ni}_5\text{P}_4$ regions, respectively. The nucleophilic P site prefer to adsorb H^* that is generated by water dissociation with an appropriate ΔG_{H^*} , thus improving the HER performance. The dehydrogenation process of adsorbed N_2H_4^* on electrophilic Co sites can be accelerated with the optimized free energy of RDS ($\text{N}_2\text{H}_4^* \rightarrow \text{N}_2\text{H}$) for enhancing of HzOR kinetics. Therefore, intelligent integration of such nucleophilic P and electrophilic Co centers into the $\text{N-Ni}_5\text{P}_4$ @CoP/CFP catalyst can achieve the high-efficient bifunctional activity toward HER and HzOR. Due to the absence of well-defined electro/nucleophilic sites, both of contrastive CoP/CFP and $\text{N-Ni}_5\text{P}_4$ /CFP exhibit the excessive bonding strength of H^* in HER and the sluggish dehydrogenation kinetics in HzOR, thus leading to the unsatisfactory bifunctional performance.

4. Conclusion

In summary, we have coupled CoP and N-doped Ni_5P_4 into a heterogeneous nanowire array grown on carbon fiber paper (named as N-

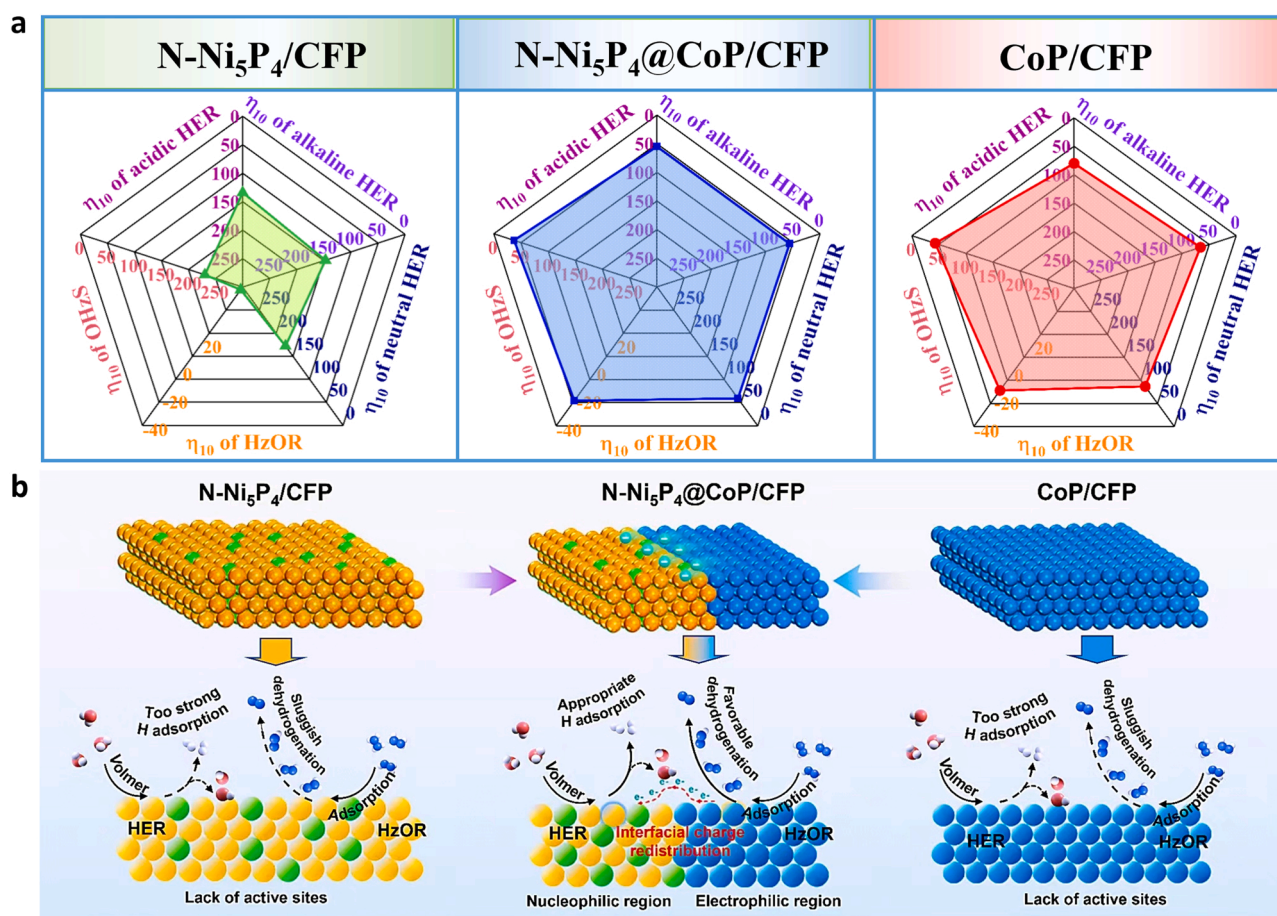


Fig. 7. (a) The radar charts of catalytic activities for $\text{N-Ni}_5\text{P}_4$ /CFP, CoP/CFP, and $\text{N-Ni}_5\text{P}_4$ @CoP/CFP. (b) Schematic illustration of HER and HzOR mechanism for $\text{N-Ni}_5\text{P}_4$ @CoP/CFP.

Ni₅P₄ @CoP/CFP), in which the Ni coordination structure is changed by selective N-doping and the energy level structure is thus tailored to significantly enhance the interfacial electronic field for improving the charge transfer from CoP to N-Ni₅P₄. The DFT calculations reveal that the nucleophilic P with more thermoneutral H* absorption energy and electrophilic Co with favorable N₂H₄ * dehydrogenation kinetics has been separately integrated in N-Ni₅P₄ and CoP components through the interfacial charge redistribution, thus leading to the booming bifunctional activity towards HER and HzOR. As a result, the overpotentials for HER to achieve 10 mA cm⁻² are as low as 55, 56, and 59 mV in acid, alkaline, and neutral media, as well as the ultralow working potential of -32 mV for HzOR to reach 10 mA cm⁻² in alkaline solution. The two-electrode OH₂S electrolyzer using the N-Ni₅P₄ @CoP/CFP catalyst as both anode and cathode requires the cell voltage of mere 0.037 V for achieving 10 mA cm⁻², much less than that of OWS system, outperforming the most recently reported OH₂S electrolyzers. Besides, the sustainable H₂ production powered by a commercial solar cell, and a home-made lemon battery can deliver a promising H₂ production rate, suggesting its great potential for energy-saving H₂ production in practical applications. Our work offers a new perspective to design the efficient catalysts toward hydrazine-assisted H₂ production by integrating electro/nucleophilic sites into heterogeneous bimetallic phosphides and sheds light on the complex relationships between surface electronic structure and function in electrocatalysis.

CRedit authorship contribution statement

Shucong Zhang: Conceptualization, Methodology, Validation, Investigation, Data curation, Writing - original draft. **Canhui Zhang:** Investigation, Data curation, Methodology, Investigation, Data curation. **Xusheng Zheng:** Investigation, Validation, Data curation. **Ge Su:** Methodology, Validation, Data Curation. **Huanlei Wang:** Data curation, Supervision. **Minghua Huang:** Conceptualization, Methodology, Validation, Writing - review & editing, Resources, Supervision.

Declaration of Competing Interest

The authors declare that they have no known competing financial interests or personal relationships that could have appeared to influence the work reported in this paper.

Data availability

Data will be made available on request.

Acknowledgements

This work was financially supported by the National Natural Science Foundation of China (22279124 and 21775142), the Natural Science Foundation of Shandong Province (ZR2020ZD10). The authors acknowledge the staff of beamline BL14W1 at the Shanghai Synchrotron Radiation Facility for their support in the XAFS measurements.

Appendix A. Supporting information

Supplementary data associated with this article can be found in the online version at [doi:10.1016/j.apcatb.2022.122207](https://doi.org/10.1016/j.apcatb.2022.122207).

References

- [1] T. Liu, A. Li, C. Wang, W. Zhou, S. Liu, L. Guo, Interfacial electron transfer of Ni₂P-NiP₂ polymorphs inducing enhanced electrochemical properties, *Adv. Mater.* 30 (2018), 1803590, <https://doi.org/10.1002/adma.201803590>.
- [2] Q. Qian, J. Zhang, J. Li, Y. Li, X. Jin, Y. Zhu, Y. Liu, Z. Li, A. El-Hairry, C. Xiao, G. Zhang, Y. Xie, Artificial heterointerfaces achieve delicate reaction kinetics towards hydrogen evolution and hydrazine oxidation catalysis, *Angew. Chem. Int. Ed.* 60 (2021) 5984–5993, <https://doi.org/10.1002/anie.202014362>.
- [3] L. Guo, Q. Yu, X. Zhai, J. Chi, T. Cui, Y. Zhang, J. Lai, L. Wang, Reduction-induced interface reconstruction to fabricate MoNi₄-based hollow nanorods for hydrazine oxidation assisted energy-saving hydrogen production in seawater, *Nano Res* 15 (2022) 8846–8856, <https://doi.org/10.1007/s12274-022-4614-x>.
- [4] Y. Liu, J. Zhang, Y. Li, Q. Qian, Z. Li, Y. Zhu, G. Zhang, Manipulating dehydrogenation kinetics through dual-doping Co₃N electrode enables highly efficient hydrazine oxidation assisting self-powered H₂ production, *Nat. Commun.* 11 (2020) 1853, <https://doi.org/10.1038/s41467-020-15563-8>.
- [5] Y. Liu, J. Zhang, Y. Li, Q. Qian, Z. Li, G. Zhang, Realizing the synergy of interface engineering and chemical substitution for Ni₃N enables its bifunctionality toward hydrazine oxidation assisted energy-saving hydrogen production, *Adv. Funct. Mater.* 31 (2021), 2103673, <https://doi.org/10.1002/adfm.202103673>.
- [6] Z. Wang, L. Xu, F. Huang, L. Qu, J. Li, K.A. Owusu, Z. Liu, Z. Lin, B. Xiang, X. Liu, K. Zhao, X. Liao, W. Yang, Y.B. Cheng, L. Mai, Copper-nickel nitride nanosheets as efficient bifunctional catalysts for hydrazine-assisted electrolytic hydrogen production, *Adv. Energy Mater.* 9 (2019), 1900390, <https://doi.org/10.1002/aenm.201900390>.
- [7] Y. Zhu, J. Zhang, Q. Qian, Y. Li, Z. Li, Y. Liu, C. Xiao, G. Zhang, Y. Xie, Dual Nanosheets on Ni/C hybrid nanosheet activate superior hydrazine oxidation assisted high-efficient H₂ production, *Angew. Chem. Int. Ed.* 61 (2022), e202113082, <https://doi.org/10.1002/anie.202113082>.
- [8] Q. Qian, W. Wang, G. Wang, X. He, Y. Feng, Z. Li, Y. Zhu, Y. Zhang, G. Zhang, Phase-selective synthesis of ruthenium phosphide in hybrid structure enables efficient hybrid water electrolysis under pH-universal conditions, *Small* 18 (2022), 2200242, <https://doi.org/10.1002/smll.202200242>.
- [9] J. Li, Y. Li, J. Wang, C. Zhang, H. Ma, C. Zhu, D. Fan, Z. Guo, M. Xu, Y. Wang, H. Ma, Elucidating the critical role of ruthenium single atom sites in water dissociation and dehydrogenation behaviors for robust hydrazine oxidation-boosted alkaline hydrogen evolution, *Adv. Funct. Mater.* 32 (2022), 2109439, <https://doi.org/10.1002/adfm.202109439>.
- [10] Y. Li, J. Li, Q. Qian, X. Jin, Y. Liu, Z. Li, Y. Zhu, Y. Guo, G. Zhang, Superhydrophilic Ni-based multicomponent nanorod-confined-nanoflake array electrode achieves waste-battery-driven hydrogen evolution and hydrazine oxidation, *Small* 17 (2021), 2008148, <https://doi.org/10.1002/smll.202008148>.
- [11] F. Sun, J. Qin, Z. Wang, M. Yu, X. Wu, X. Sun, J. Qiu, Energy-saving hydrogen production by chlorine-free hybrid seawater splitting coupling hydrazine degradation, *Nat. Commun.* 12 (2021) 4182, <https://doi.org/10.1038/s41467-021-24529-3>.
- [12] H. Liu, M. Jin, D. Zhan, J. Wang, X. Cai, Y. Qiu, L. Lai, Stacking faults triggered strain engineering of ZIF-67 derived Ni-Co bimetal phosphide for enhanced overall water splitting, *Appl. Catal., B* 272 (2020), 118951, <https://doi.org/10.1016/j.apcatb.2020.118951>.
- [13] L. Yu, J. Zhang, Y. Dang, J. He, Z. Tobin, P. Kerns, Y. Dou, Y. Jiang, Y. He, S.L. Suib, In situ growth of Ni₂P-Cu₃P bimetallic phosphide with bicontinuous structure on self-supported NiCuC substrate as an efficient hydrogen evolution reaction electrocatalyst, *ACS Catal.* 9 (2019) 6919–6928, <https://doi.org/10.1021/acscatal.9b00494>.
- [14] F. Yu, H. Zhou, Y. Huang, J. Sun, F. Qin, J. Bao, W.A. Goddard, S. Chen, Z. Ren, High-performance bifunctional porous non-noble metal phosphide catalyst for overall water splitting, *Nat. Commun.* 9 (2018) 2551, <https://doi.org/10.1038/s41467-018-04746-z>.
- [15] L. Wu, L. Yu, F. Zhang, B. McElhenny, D. Luo, A. Karim, S. Chen, Z. Ren, Heterogeneous bimetallic phosphide Ni₂P-Fe₂P as an efficient bifunctional catalyst for water/seawater splitting, *Adv. Funct. Mater.* 31 (2021), 2006484, <https://doi.org/10.1002/adfm.202006484>.
- [16] P. Tang, H. Wen, C. Chen, X. Lin, P. Wang, Hierarchically nanostructured (Ni, Co) phosphides for hydrazine electrooxidation, *Electro Acta* 387 (2021), 138492, <https://doi.org/10.1016/j.electacta.2021.138492>.
- [17] H. Wen, L. Gan, H. Dai, X. Wen, L. Wu, H. Wu, Ping Wang, In situ grown Ni phosphide nanowire array on Ni foam as a high-performance catalyst for hydrazine electrooxidation, *Appl. Catal., B* 241 (2019) 292–298, <https://doi.org/10.1016/j.apcatb.2018.09.043>.
- [18] L. Zhai, X. She, L. Zhuang, Y. Li, R. Ding, X. Guo, Y. Zhang, Y. Zhu, K. Xu, H.J. Fan, S.P. Lau, Modulating built-in electric field via variable oxygen affinity for robust hydrogen evolution reaction in neutral media, *Angew. Chem. Int. Ed.* 61 (2022), e202116057, <https://doi.org/10.1002/anie.202116057>.
- [19] S. Ni, H. Qu, Z. Xu, X. Zhu, H. Xing, L. Wang, J. Yu, H. Liu, C. Chen, L. Yang, Interfacial engineering of the NiSe₂/FeSe₂ p-p heterojunction for promoting oxygen evolution reaction and electrocatalytic urea oxidation, *Appl. Catal., B* 299 (2021), 120638, <https://doi.org/10.1016/j.apcatb.2021.120638>.
- [20] Y. Shi, W. Du, W. Zhou, C. Wang, S. Lu, S. Lu, B. Zhang, Unveiling the promotion of surface-adsorbed chalcogenate on the electrocatalytic oxygen evolution reaction, *Angew. Chem. Int. Ed.* 59 (2020) 22470–22474, <https://doi.org/10.1002/anie.202011097>.
- [21] J. Li, S. Wang, J. Chang, L. Feng, A review of Ni based powder catalyst for urea oxidation in assisting water splitting reaction, *Adv. Powder Mater.* 1 (2022), 100030, <https://doi.org/10.1016/j.jpamate.2022.01.003>.
- [22] S. Niu, Y. Fang, D. Rao, G. Liang, S. Li, J. Cai, B. Liu, J. Li, G. Wang, Reversing the nucleophilicity of active sites in CoP₂ enables exceptional hydrogen evolution catalysis, *Small* 18 (2022), 2106870, <https://doi.org/10.1002/smll.202106870>.
- [23] W. Wang, Y. Wang, R. Yang, Q. Wen, Y. Liu, Z. Jiang, H. Li, T. Zhai, Vacancy-rich Ni(OH)₂ drives the electrooxidation of amino C-N bonds to nitrile C≡N Bonds, *Angew. Chem. Int. Ed.* 59 (2020) 16974–16981, <https://doi.org/10.1002/anie.202005574>.
- [24] H. Yu, J. Huang, L. Jiang, L. Leng, K. Yi, W. Zhang, C. Zhang, X. Yuan, In situ construction of Sn-doped structurally compatible heterojunction with enhanced

- interfacial electric field for photocatalytic pollutants removal and CO₂ reduction, *Appl. Catal., B* 298 (2021), 120618, <https://doi.org/10.1016/j.apcatb.2021.120618>.
- [25] Y. Sun, X. Li, T. Zhang, K. Xu, Y. Yang, G. Chen, C. Li, Y. Xie, Nitrogen-doped cobalt diselenide with cubic phase maintained for enhanced alkaline hydrogen evolution, *Angew. Chem. Int. Ed.* 60 (2021) 21575–21582, <https://doi.org/10.1002/anie.202109116>.
- [26] S. Zhang, T. Xiong, X. Tang, Q. Ma, F. Hu, Y. Mi, Engineering inner-porous cobalt phosphide nanowire based on controllable phosphating for efficient hydrogen evolution in both acidic and alkaline conditions, *Appl. Surf. Sci.* 481 (2019) 1524–1531, <https://doi.org/10.1016/j.apsusc.2019.03.250>.
- [27] S. Zhang, W. Wang, F. Hu, Y. Mi, S. Wang, Y. Liu, X. Ai, J. Fang, H. Li, T. Zhai, 2D CoOOH sheet-encapsulated Ni₂P into tubular arrays realizing 1000 mA cm⁻²-level-current-density hydrogen evolution over 100h in neutral water, *Nano-Micro Lett.* 12 (2020) 140, <https://doi.org/10.1007/s40820-020-00476-4>.
- [28] X. Shan, J. Liu, H. Mu, Y. Xiao, B. Mei, W. Liu, G. Lin, Z. Jiang, L. Wen, L. Jiang, An engineered superhydrophilic/superaerophobic electrocatalyst composed of the supported CoMoS_x chalcogen for overall water splitting, *Angew. Chem. Int. Ed.* 59 (2020) 1659–1665, <https://doi.org/10.1002/anie.201911617>.
- [29] W. Hong, C. Lv, S. Sun, G. Chen, Fabrication and study of the synergistic effect of Janus Ni₂P/Ni₃P₄ embedded in N-doped carbon as efficient electrocatalysts for hydrogen evolution reaction, *Catal. Sci. Technol.* 10 (2020) 1023–1029, <https://doi.org/10.1039/C9CY01918A>.
- [30] H. Jin, X. Wang, C. Tang, A. Vasileff, L. Li, A. Slattery, S.Z. Qiao, Stable and highly efficient hydrogen evolution from seawater enabled by an unsaturated nickel surface nitride, *Adv. Mater.* 33 (2021), 2007508, <https://doi.org/10.1002/adma.202007508>.
- [31] J. Cai, Y. Zhang, S. Niu, Y. Wu, Y. Xie, X. Zheng, Y. Liu, Y. Lin, X. Liu, G. Wang, Y. Qian, N-induced lattice contraction generally boosts the hydrogen evolution catalysis of P-rich metal phosphides, *Sci. Adv.* 6 (2020) eaaw8113, <https://doi.org/10.1126/sciadv.aaw8113>.
- [32] T. Wang, M. Wang, H. Yang, M. Xu, C. Zuo, K. Feng, M. Xie, J. Deng, J. Zhong, W. Zhou, T. Cheng, Y. Li, Weakening hydrogen adsorption on nickel via interstitial nitrogen doping promotes bifunctional hydrogen electrocatalysis in alkaline solution, *Energy Environ. Sci.* 12 (2019) 3522–3529, <https://doi.org/10.1039/C9EE01743G>.
- [33] Y. Pan, K. Sun, Y. Lin, X. Cao, Y. Cheng, S. Liu, L. Zeng, W. Cheong, D. Zhao, K. Wu, Z. Liu, Y. Liu, D. Wang, Q. Peng, C. Chen, Y. Li, Electronic structure and d-band center control engineering over M-doped CoP (M = Ni, Mn, Fe) hollow polyhedron frames for boosting hydrogen production, *Nano Energy* 56 (2019) 411–419, <https://doi.org/10.1016/j.nanoen.2018.11.034>.
- [34] I. Mishra, H. Zhou, J. Sun, F. Qin, K. Dahal, J. Bao, S. Chen, Z. Ren, Hierarchical CoP/Ni₃P₄/CoP microsheet arrays as a robust pH-universal electrocatalyst for efficient hydrogen generation, *Energy Environ. Sci.* 11 (2018) 2246–2252, <https://doi.org/10.1039/C8EE01270A>.
- [35] X. Huang, X. Xu, C. Li, D. Wu, D. Cheng, D. Cao, Vertical CoP nanoarray wrapped by N, P-doped carbon for hydrogen evolution reaction in both acidic and alkaline conditions, *Adv. Energy Mater.* 9 (2019), 1803970, <https://doi.org/10.1002/aenm.201803970>.
- [36] N. Zhang, Y. Zou, L. Tao, W. Chen, L. Zhou, Z. Liu, B. Zhou, G. Huang, H. Lin, S. Wang, Electrochemical oxidation of 5-hydroxymethylfurfural on nickel nitride/carbon nanosheets: reaction pathway determined by in situ sum frequency generation vibrational spectroscopy, *Angew. Chem. Int. Ed.* 58 (2019) 15895–15903, <https://doi.org/10.1002/anie.201908722>.
- [37] F. Lin, H. Qin, T. Wang, L. Yang, X. Cao, L. Jiao, Few-layered MoN-MnO, Heterostruct. Interfacial-O Synerg. Act. Cent. Boost. Electro Hydrog. Evol., *J. Mater. Chem. A* 9 (2021) 8325–8331, <https://doi.org/10.1039/D1TA00908G>.
- [38] J.X. Feng, H. Xu, S.H. Ye, G. Ouyang, Y.X. Tong, G.R. Li, Silica-polypyrrole hybrids as high-performance metal-free electrocatalysts for the hydrogen evolution reaction in neutral media, *Angew. Chem. Int. Ed.* 56 (2017) 8120–8124, <https://doi.org/10.1002/anie.201702934>.
- [39] C.F. Fu, X. Wu, J. Yang, Material design for photocatalytic water splitting from a theoretical perspective, *Adv. Mater.* 30 (2018), 1802106, <https://doi.org/10.1002/adma.201802106>.
- [40] S. Shen, Z. Lin, K. Song, Z. Wang, L. Huang, L. Yan, F. Meng, Q. Zhang, L. Gu, W. Zhong, Reversed active sites boost the intrinsic activity of graphene-like cobalt selenide for hydrogen evolution, *Angew. Chem. Int. Ed.* 60 (2021) 12360–12365, <https://doi.org/10.1002/anie.202102961>.
- [41] K.L. Zhou, Z. Wang, C.B. Han, X. Ke, C. Wang, Y. Jin, Q. Zhang, J. Liu, H. Wang, H. Yan, Platinum single-atom catalyst coupled with transition metal/metal oxide heterostructure for accelerating alkaline hydrogen evolution reaction, *Nat. Commun.* 12 (2021) 3783, <https://doi.org/10.1038/s41467-021-24079-8>.
- [42] H. Zhou, Y. Ren, Z. Li, M. Xu, Y. Wang, R. Ge, X. Kong, L. Zheng, H. Duan, Electrocatalytic upcycling of polyethylene terephthalate to commodity chemicals and H₂ fuel, *Nat. Commun.* 12 (2021) 4679, <https://doi.org/10.1038/s41467-021-25048-x>.
- [43] X. Jiang, H. Jang, S. Liu, Z. Li, M.G. Kim, C. Li, Q. Qin, X. Liu, J. Cho, The heterostructure of Ru₂P/VO₃/NPC synergistically promotes H₂O dissociation for improved hydrogen evolution, *Angew. Chem. Int. Ed.* 60 (2021) 4110–4116, <https://doi.org/10.1002/anie.202014411>.
- [44] Q. Dai, L. Wang, K. Wang, X. Sang, Z. Li, B. Yang, J. Chen, L. Lei, L. Dai, Y. Hou, Accelerated water dissociation kinetics by electron-enriched cobalt sites for efficient alkaline hydrogen evolution, *Adv. Funct. Mater.* 32 (2022), 2109556, <https://doi.org/10.1002/adfm.202109556>.
- [45] P. Chen, K. Xu, Z. Fang, Y. Tong, J. Wu, X. Lu, X. Peng, H. Ding, C. Wu, Y. Xie, Metallic Co₄N porous nanowire arrays activated by surface oxidation as electrocatalysts for the oxygen evolution reaction, *Angew. Chem. Int. Ed.* 54 (2015) 14710–14714, <https://doi.org/10.1002/anie.201506480>.
- [46] Y. Wu, X. Liu, D. Han, X. Song, L. Shi, Y. Song, S. Niu, Y. Xie, J. Cai, S. Wu, J. Kang, J. Zhou, Z. Chen, X. Zheng, X. Xiao, G. Wang, Electron density modulation of NiCo₂S₄ nanowires by nitrogen incorporation for highly efficient hydrogen evolution catalysis, *Nat. Commun.* 9 (2018) 1425, <https://doi.org/10.1038/s41467-018-03858-w>.
- [47] Z.P. Wu, H. Zhang, S. Zuo, Y. Wang, S.L. Zhang, J. Zhang, S.Q. Zang, X.W. Lou, Manipulating the local coordination and electronic structures for efficient electrocatalytic oxygen evolution, *Adv. Mater.* 33 (2021), 2103004, <https://doi.org/10.1002/adma.202103004>.
- [48] Q. Wen, K. Yang, D. Huang, G. Cheng, X. Ai, Y. Liu, J. Fang, H. Li, L. Yu, T. Zhai, Schottky heterojunction nanosheet array achieving high-current-density oxygen evolution for industrial water splitting electrolyzers, *Adv. Energy Mater.* 11 (2021), 2102353, <https://doi.org/10.1002/aenm.202102353>.
- [49] G. Yang, Y. Jiao, H. Yan, Y. Xie, A. Wu, X. Dong, D. Guo, C. Tian, H. Fu, Interfacial engineering of MoO₂-FeP heterojunction for highly efficient hydrogen evolution coupled with biomass electrooxidation, *Adv. Mater.* 32 (2020), 2000455, <https://doi.org/10.1002/adma.202000455>.
- [50] J. Sun, H. Xue, N. Guo, T. Song, Y.R. Hao, J. Sun, J. Zhang, Q. Wang, Synergetic metal defect and surface chemical reconstruction into NiCo₂S₄/ZnS heterojunction to achieve outstanding oxygen evolution performance, *Angew. Chem. Int. Ed.* 60 (2021) 19435–19441, <https://doi.org/10.1002/anie.202107731>.
- [51] Z. Zhou, Y. Kong, H. Tan, Q. Huang, C. Wang, Z. Pei, H. Wang, Y. Liu, Y. Wang, S. Li, X. Liao, W. Yan, S. Zhao, Cation-vacancy-enriched nickel phosphide for efficient electrosynthesis of hydrogen peroxides, *Adv. Mater.* 34 (2022), 2106541, <https://doi.org/10.1002/adma.202106541>.
- [52] J. Liu, C. Tang, Z. Ke, R. Chen, H. Wang, W. Li, C. Jiang, D. He, G. Wang, X. Xiao, Optimizing hydrogen adsorption by d-d orbital modulation for efficient hydrogen evolution catalysis, *Adv. Energy Mater.* 12 (2022), 2103301, <https://doi.org/10.1002/aenm.202103301>.
- [53] W. Li, S. Xue, S. Watzel, S. Hou, J. Fichtner, A.L. Semrau, L. Zhou, A. Welle, A. S. Bandarenka, R.A. Fischer, Advanced bifunctional oxygen reduction and evolution electrocatalyst derived from surface-mounted metal-organic frameworks, *Angew. Chem. Int. Ed.* 59 (2020) 5837–5843, <https://doi.org/10.1002/anie.201916507>.
- [54] J. Zhou, Z. Han, X. Wang, H. Gai, Z. Chen, T. Guo, X. Hou, L. Xu, X. Hu, M. Huang, S.V. Levchenko, H. Jiang, Discovery of quantitative electronic structure-OER activity relationship in metal-organic framework electrocatalysts using an integrated theoretical-experimental approach, *Adv. Funct. Mater.* 31 (2021), 2102066, <https://doi.org/10.1002/adfm.202102066>.
- [55] X. Fang, L. Ren, F. Li, Z. Jiang, Z. Wang, Modulating electronic structure of CoSe₂ by Ni doping for efficient electrocatalyst for hydrogen evolution reaction, *Rare Met* 41 (2022) 901–910, <https://doi.org/10.1007/s12598-021-01819-9>.
- [56] B.H.R. Suryanto, Y. Wang, R.K. Hocking, W. Adamson, C. Zhao, Overall electrochemical splitting of water at the heterogeneous interface of nickel and iron oxide, *Nat. Commun.* 10 (2019) 5599, <https://doi.org/10.1038/s41467-019-13415-8>.
- [57] X. Liu, J. He, S. Zhao, Y. Liu, Z. Zhao, J. Luo, G. Hu, X. Sun, Y. Ding, Self-powered H₂ production with bifunctional hydrazine as sole consumable, *Nat. Commun.* 9 (2018) 4365, <https://doi.org/10.1038/s41467-018-06815-9>.
- [58] D. Liu, J.C. Liu, W. Cai, J. Ma, H.B. Yang, H. Xiao, J. Li, Y. Xiong, Y. Huang, B. Liu, Selective photoelectrochemical oxidation of glycerol to high value-added dihydroxyacetone, *Nat. Commun.* 10 (2019) 1779, <https://doi.org/10.1038/s41467-019-09788-5>.
- [59] T. Zhao, X. Shen, Y. Wang, R.K. Hocking, Y. Li, C. Rong, K. Dastafkan, Z. Su, C. Zhao, In situ reconstruction of V-doped Ni₂P pre-Catalysts with tunable electronic structures for water oxidation, *Adv. Funct. Mater.* 31 (2021), 2100614, <https://doi.org/10.1002/adfm.202100614>.
- [60] H.Y. Wang, S.F. Hung, H.Y. Chen, T.S. Chan, H.M. Chen, B. Liu, In operando identification of geometrical-site-dependent water oxidation activity of spinel Co₃O₄, *J. Am. Chem. Soc.* 138 (2016) 36–39, <https://doi.org/10.1021/jacs.5b10525>.